

# A $\sim 75$ per cent occurrence rate of debris discs around F stars in the $\beta$ Pic moving group

Nicole Pawellek<sup>1,2\*</sup>, Mark Wyatt<sup>1</sup>, Luca Matrà<sup>3</sup>, Grant Kennedy<sup>4</sup> and Ben Yelverton<sup>1</sup>

<sup>1</sup>*Institute of Astronomy, University of Cambridge, Madingley Road, Cambridge CB3 0HA, UK*

<sup>2</sup>*Konkoly Observatory, Research Centre for Astronomy and Earth Sciences, Konkoly-Thege Miklós út 15-17, H-1121 Budapest, Hungary*

<sup>3</sup>*School of Physics, National University of Ireland Galway, University Road, Galway, Ireland*

<sup>4</sup>*Department of Physics and Centre for Exoplanets and Habitability, University of Warwick, Gibbet Hill Road, Coventry CV4 7AL, UK*

Accepted 2021 January 28. Received 2021 January 28; in original form 2020 October 30

## ABSTRACT

Only 20 per cent of old field stars have detectable debris discs, leaving open the question of what disc, if any, is present around the remaining 80 per cent. Young moving groups allow to probe this population, since discs are expected to have been brighter early on. This paper considers the population of F stars in the 23 Myr-old  $\beta$  Pictoris moving group (BPMG) where we find that 9/12 targets possess discs. We also analyse archival ALMA data to derive radii for four of the discs, presenting the first image of the 63 au radius disc of HD 164249. Comparing the BPMG results to disc samples from  $\sim 45$ -Myr and  $\sim 150$ -Myr-old moving groups, and to discs found around field stars, we find that the disc incidence rate in young moving groups is comparable to that of the BPMG and significantly higher than that of field stars. The BPMG discs tend to be smaller than those around field stars. However, this difference is not statistically significant due to the small number of targets. Yet, by analysing the fractional luminosity versus disc radius parameter space, we find that the fractional luminosities in the populations considered drop by two orders of magnitude within the first 100 Myr. This is much faster than expected by collisional evolution, implying a decay equivalent to  $1/\text{age}^2$ . We attribute this depletion to embedded planets, which would be around  $170 M_{\text{earth}}$  to cause a depletion on the appropriate time-scale. However, we cannot rule out that different birth environments of nearby young clusters result in brighter debris discs than the progenitors of field stars that likely formed in a more dense environment.

**Key words:** stars HD 14082A, HD15115, HD 29391, HD 35850, HD 160305, HD 164249, HD 173167, HD 181327, HD 191089, HD 199143, HD 213429 – planets and satellites: physical evolution – planet–disc interactions – infrared: planetary systems.

## 1 INTRODUCTION

After its protoplanetary disc has dispersed, a star is left with – if anything – a system of planets and debris belts. The dust in those debris belts is inferred to originate in the breakup of planetesimals at least kilometres in size (e.g. Wyatt 2008; Krivov 2010; Hughes, Duchêne & Matthews 2018) and is seen in far-infrared (FIR) surveys towards  $\sim 20$  per cent of nearby several Gyr-old stars (e.g. Eiroa et al. 2013; Sibthorpe et al. 2018), where a slightly higher detection rate is noted for earlier-type stars (e.g. Su et al. 2006; Sibthorpe et al. 2018).

FIR surveys of nearby stars also show that debris disc luminosities decrease with age in a manner explained by population models in which all stars are born with a debris belt that is depleted by collisions among the planetesimals (Wyatt et al. 2007; Gáspár, Rieke & Balog 2013). This canonical model successfully explains the detection statistics (as a function of wavelength and stellar age), with the implication that all stars are born with a planetesimal belt of initial mass drawn from a lognormal distribution like that of protoplanetary discs and concentrated at a radius drawn from a  $n(r) \propto r^{-1.7}$  distribution in the range of 1–1000 au (Sibthorpe et al. 2018).

However, while this model makes accurate predictions for the 20 per cent of Gyr-old stars with detectable discs, it is almost completely unconstrained for the 80 per cent of stars without detectable discs for which model predictions rely on the lognormal or power-law assumptions about the underlying initial mass and radius distributions. For example, stars in the canonical model population without detectable discs are the 80 per cent with 1–10 au discs that are rapidly depleted and so never seen, whereas it would be equally valid to put these undetected discs at 30–100 au with very low initial mass. A further challenge comes from the inference that planetesimal belt radii depend on stellar luminosity. Belts imaged at millimetre wavelengths are larger around higher luminosity stars in a way that may be attributed to preferential formation at protoplanetary disc ice-lines (Matrà et al. 2018), a possibility not currently included in the model.

It is inevitably challenging to determine the properties of the planetesimal belts of the 80 per cent of nearby stars without detectable dust. Our only hope is to probe these by studying stars that are young ( $\ll 100$  Myr when their discs are brightest) and nearby. Young nearby moving groups are ideal for sample selection, having also the benefit of being coeval. Given the stellar luminosity dependence mentioned above, and that disc detection is maximized

\* E-mail: pawellek@ast.cam.ac.uk

**Table 1.** Stellar parameters of the sample of 12 F-type stars belong to the  $\beta$  Pic moving group.

HD	HIP	SpT	$L/L_{\text{sun}}$	$T_{\text{eff}}$ (K)	d (pc)	Companion	Multiplicity SpT	Separation (arcsec)	Ref.	Planetary companion Separation (au)	Mass ( $M_{\text{Jup}}$ )
203	560	F2V	$4.26 \pm 0.03$	$6830 \pm 30$	40.0	–	–	–	–	–	–
14082A	10680	F5V	$2.00 \pm 0.01$	$6170 \pm 20$	39.8	HD 14082B	G2V	14	557	1, 4	–
15115	11360	F4V	$3.6 \pm 0.1$	$6720 \pm 20$	49.0	–	–	–	–	–	–
29391 <sup>a</sup>	21547	F0V	$5.71 \pm 0.06$	$7330 \pm 30$	29.8	GJ 3305AB	M1V	66	1957	1	13
35850	25486	F8V	$1.84 \pm 0.01$	$6050 \pm 20$	26.9	HD 35850B	–	$7.8 \times 10^{-4}$	0.021	6, 7	–
160305	86598	F9V	$1.69 \pm 0.03$	$6050 \pm 40$	65.7	–	–	–	–	–	–
164249	88399	F5V	$3.20 \pm 0.04$	$6340 \pm 40$	49.6	HD 164249B	M2V	6.5	323	1	–
						2MASS J18011138-5125594	–	–	3	–	–
173167	–	F5V	$2.4 \pm 0.1$	$6270 \pm 90$	50.6	TYC 9073-0762	M1V	571	28894	1, 2	–
181327	95270	F5V	$2.87 \pm 0.02$	$6480 \pm 20$	48.2	HD181296	A0V+M7/8V	416	20072	1	–
191089	99273	F5V	$2.74 \pm 0.02$	$6460 \pm 30$	50.1	–	–	–	–	–	–
199143	103311	F8V	$2.21 \pm 0.02$	$5930 \pm 20$	45.7	HD 199143B	M2V	1.1	50	4, 8	–
						HD 358623	K7	325.0	14764	1, 8	–
213429	111170	F8V	$1.92 \pm 0.06$	$5970 \pm 20$	25.5	HD 213429B	–	$\sim 0.08^b$	$\sim 2^b$	1, 5	–

<sup>a</sup>HD 29391 is also known as 51 Eridani. The references for the planetary companion are given in Section 2.3. <sup>b</sup>The orbital period is 631 d. It is converted to a separation assuming the mass of the binary companion to be equal to that of the primary HD 213429 with  $1.19 M_{\odot}$ .

References for multiplicity: (1) Elliott & Bayo (2016), (2) Moór et al. (2013), (3) Gagné et al. (2018a), (4) Mamajek & Bell (2014), (5) Kovaleva et al. (2015), (6) Eker et al. (2008), (7) Rodriguez & Zuckerman (2012), and (8) Tokovinin (1997).

for higher luminosity stars, the optimal sample would include stars of similar early spectral type in the nearest youngest moving group. The number of A-type stars in nearby young moving groups for which the disc detection peaks is very limited while late-type stars are common. The best compromise between a high stellar luminosity and a reasonably large number of targets within the same moving group is given by F-type stars.

An example fulfilling the aforementioned requirements is the  $\beta$  Pictoris moving group (BPMG), which contains stars of  $\sim 23$  Myr age (Bell, Mamajek & Naylor 2015). Based on a survey of 30 BPMG stars of different spectral types, Rebull et al. (2008) found that more than 37 per cent of the targets show evidence for a circumstellar disc. By considering the known F-type stars in the BPMG, Churcher, Wyatt & Smith (2011) inferred a debris disc detection rate of 6/9 ( $\sim 67$  per cent). This is higher than the 20 per cent seen for Gyr-old stars (e.g. Su et al. 2006; Marshall et al. 2016; Sibthorpe et al. 2018) leading to the question why we get such a high frequency. One explanation could be that during the time span of two orders of magnitude in age ( $\sim 20$  Myr and  $\sim 2$  Gyr), a majority of discs is collisionally depleted so that we are not able to detect them anymore. Another possibility might be that the formation conditions of the BPMG differ significantly from these field stars leading to debris discs having atypical properties (i.e. unusually bright).

In the first part of this study, we consider the population of F-star debris discs in the BPMG. In Section 2, we revisit membership in the BPMG sample in the light of recent studies and note stellar multiplicity and planetary companions for the sample since those are possible influences on the occurrence of discs. We investigate evidence for infrared excesses indicative of a surrounding debris disc in Section 3, then Section 4 presents Atacama Large Millimeter/submillimeter Array (ALMA) observations to determine the radii of the belts. We use this spatial information to generate spectral energy distribution (SED) models including a size distribution of dust particles in Section 5.

In the second part of this study, the properties of the BPMG disc population are compared with those of other nearby F-star populations in Section 6 to identify similarities and differences between the samples. In Section 7, we analyse possible scenarios explaining the high detection rate of F-star debris discs in the BPMG, before concluding in Section 8.

## 2 SAMPLE SELECTION

### 2.1 Reassessing the BPMG sample of F stars

The BPMG is one of the nearest moving groups. Shkolnik et al. (2017) identified 146 objects belonging to this group, where five stars are found to be A-type, 11 F-type, six G-type, 27 K-type, and 97 M- and L-type. Using data from the *Gaia* data release 2 (Gaia Collaboration 2018), several additional members of the BPMG were found by Gagné & Faherty (2018). While the majority found in that study are M- and L-type, one F-type star and one A-type star could also be added to the sample given by Shkolnik et al. (2017). Thus, the sample of nine F-type members of the BPMG analysed by Churcher et al. (2011) is now increased to 12 by combining the samples of Shkolnik et al. (2017) and Gagné & Faherty (2018). These 12 targets will be the basis of our analysis. All of them lie between 25 and 66 pc (Gaia Collaboration 2018; Bailer-Jones et al. 2018), with stellar properties listed in Table 1.

### 2.2 Stellar multiplicity

Investigating the stellar multiplicity, we found that our sample of F stars possesses a 67 per cent fraction of multiple systems (8/12) including wide (separations  $> 1000$  au) and very wide systems (separations  $> 10\,000$  au). Elliott & Bayo (2016) studied the occurrence of such system configurations and found that the high fraction of multiples in the BPMG can be explained by the unfolding of primordial triple systems, which was investigated by Reipurth & Mikkola (2012). The term ‘unfolding’ means that in triple systems, while born compact, one component is dynamically scattered into a very distant orbit within a few Myr. Reipurth & Mikkola (2012) showed that if the component scattered into a wide separation is of low mass while the close components are more massive, the triple system is likely to be unstable and disrupted on a short time-scale into a massive binary system and a single low-mass star. Elliott & Bayo (2016) find that the majority of the multiples’ distant components in the BPMG are of low mass and, therefore, the study predicts that these multiple systems should decay within 100 Myr. In our sample, the systems with low-mass binary companions are HD 29391, HD 164249, HD 173167, and HD 199143 for which we might expect a decay within the aforementioned time frame.

**Table 2.** IR excesses.

HD	WISE22			MIPS24			MIPS70			PACS70			PACS100		
	$F_\nu$ (mJy)	$F_{\nu,*}$ (mJy)	Excess $\sigma$	$F_\nu$ (mJy)	$F_{\nu,*}$ (mJy)	Excess $\sigma$	$F_\nu$ (mJy)	$F_{\nu,*}$ (mJy)	Excess $\sigma$	$F_\nu$ (mJy)	$F_{\nu,*}$ (mJy)	Excess $\sigma$	$F_\nu$ (mJy)	$F_{\nu,*}$ (mJy)	Excess $\sigma$
203	126.5 ± 7.2	64.2	8.6	120.5 ± 2.4	55.9	27	61.0 ± 10.4	6.1	5.3	71.5 ± 4.4	6.4	15	41.3 ± 2.5	3.2	15
14082A	64.1 ± 3.8	41.3	6.0*	39.9 ± 0.8	36.0	4.9*	—	—	3.9	<13	4.1	—	<8	2.0	—
15115	63.1 ± 3.8	39.0	6.3	58.3 ± 2.3	33.9	11	451.9 ± 32.6	3.7	14	463.0 ± 14.5	3.9	32	—	1.9	—
29391	141.8 ± 8.0	123	2.3	129.7 ± 2.6	107	8.8	23.0 ± 0.92	11.5	12	21.8 ± 3.8	12.2	2.5	19.0 ± 3.0	6.0	4.3
35850	96.9 ± 5.7	87.5	1.6	83.5 ± 3.4	76.2	2.1	40.3 ± 9.20	8.3	3.5	—	8.8	—	46.1 ± 2.6	4.3	16
160305	18.5 ± 1.7	13.2	3.1	—	11.5	—	—	1.3	—	31.9 ± 1.6	1.3	18	—	0.65	—
164249	85.4 ± 5.1	39.2	9.0	77.4 ± 1.6	34.1	28	624.1 ± 62.4	4.1	10	—	3.9	—	513.0 ± 17.7	1.9	29
173167	33.9 ± 2.2	29.3	2.0	—	25.5	—	—	3.7	—	—	2.9	—	—	1.4	—
181327	212.2 ± 12.1	34.6	15	205.4 ± 4.1	30.1	43	1468 ± 249	3.3	5.9	—	3.5	—	1463 ± 47	1.7	31
191089	192.8 ± 10.9	30.9	15	187.5 ± 3.8	26.9	43	544.3 ± 50.6	2.9	11	—	3.1	—	422.6 ± 13.5	1.5	31
199143	45.2 ± 2.9	37.8	2.5	38.8 ± 0.9	32.9	7.0	<9	3.6	—	4.89 ± 1.37	3.8	0.80	—	1.9	—
213429	107.3 ± 6.3	105	0.40	93.1 ± 1.9	91.2	1.0	22.2 ± 4.1	10.0	2.9	—	10.5	—	—	5.2	—

*Note.* Errors include both statistical and systematic uncertainties. WISE data from WISE All-Sky Catalog (Wright et al. 2010), MIPS24 and MIPS70 from Spitzer Heritage Archive (Carpenter et al. 2008; Chen et al. 2014; Sierchio et al. 2014), and PACS70 and PACS100 from Herschel Science Archive (Eiroa et al. 2013). Upper limits stem from Riviere-Marichalar et al. (2014). The thermal emission caused by the dust material surrounding the star is given as excess from the stellar photosphere in units of  $\sigma$  and is considered to be significant if it reaches a value larger than 3. (\*) The WISE and MIPS data of HD 14082A were found to be confused and thus are not taken into account when checking the presence of IR excess.

## 2.3 Planetary companions

In our sample of F stars, only the most luminous star HD 29391, also known as 51 Eridani, is known to possess a planetary companion (e.g. Macintosh et al. 2015; Nielsen et al. 2019). The system is located at a distance of 29.8 pc and forms a multiple stellar system with the M-type binary star GJ 3305AB (e.g. Janson et al. 2014). The companion 51 Eri b was discovered by the Gemini Planet Imager Exoplanet Survey (GPIS, Patience et al. 2015; Nielsen et al. 2019) with a projected separation of 13 au. Depending on the formation model, the estimated mass of the planet varies between  $1...2M_{\text{Jup}}$  for a so-called ‘hot start’ model (Marley et al. 2007; Rajan et al. 2017) and  $2...12M_{\text{Jup}}$  for a ‘cold start’ model (Marley et al. 2007; Fortney et al. 2008).

## 3 ASSESSING THE SAMPLE FOR IR EXCESS

### 3.1 Modelling procedure

We collected photometric data for all 12 targets in our sample from published catalogues, such as 2MASS (Cutri et al. 2003), the WISE All-Sky Release Catalog (Wright et al. 2010), the AKARI All-Sky Catalogue (Ishihara et al. 2010), the Spitzer Heritage Archive (Carpenter et al. 2008; Leboutteiller et al. 2011; Chen et al. 2014; Sierchio et al. 2014), and the Herschel Point Source Catalogue (Marton et al. 2015). These data allowed us to analyse the SEDs and therefore the occurrence of infrared emission in excess of that expected from the stellar photosphere. Mid- and far-infrared excesses are an indicator of the presence of a debris disc surrounding a host star.

To find excesses, we fit a SED model consisting of a star and a disc. We fit PHOENIX stellar photosphere models (Brott & Hauschildt 2005) for each target using the stellar luminosity and the stellar temperature as model parameters. The resulting stellar luminosities and temperatures are listed in Table 1. Knowing the stellar contribution to the mid- and far-infrared data, we were able to derive the excess emission in the appropriate wavelength bands between 22 and 100  $\mu\text{m}$  taking into account the uncertainties of the photometry and the photospheric model (Yelverton et al. 2019). The results are given in Table 2.

After subtracting the stellar emission, the disc is fitted with a modified blackbody model (Backman & Paresce 1993) for which

the thermal emission of the dust is described as

$$F_\nu \sim B_\nu(\lambda, T_{\text{dust}}) \left[ H(\lambda_0 - \lambda) + H(\lambda - \lambda_0) \left( \frac{\lambda}{\lambda_0} \right)^{-\beta} \right], \quad (1)$$

where  $B_\nu$  is the Planck function and  $H$  the Heaviside step function. The parameter  $\lambda_0$  represents the characteristic wavelength while  $\beta$  is the opacity index. From this model, we derive the dust temperature,  $T_{\text{BB}}$ , and the resulting blackbody radius of the disc,  $R_{\text{BB}}$ , as well as the fractional luminosity,  $f_d$  (see Fig. 1 and Table 3). Here,  $R_{\text{BB}}$  is the distance from the star that the temperature implies if the dust acted like blackbodies in equilibrium with the stellar radiation. In Section 5, we apply a disc model including dust-size distributions, which do not exist in the framework of Yelverton et al. (2019).

The uncertainties of the fit parameters were inferred in the following way. We start at the position of the minimum  $\chi^2$  in parameter space, i.e. from the best-fitting  $f_d$  and  $R_{\text{BB}}$ . A set of new parameter values is randomly generated from which we calculate the SED. This leads to a new  $\chi^2$  value, which is compared to the former minimum value. The  $\chi^2$  parameter estimates how likely the set of parameter values fits the SED. If the probability is larger than a certain threshold value, the set is saved. In the end, it is counted how often the code reaches a certain set of  $f_d$  and  $R_{\text{BB}}$ . The closer the parameters get to the best-fitting values, the higher the probability. The resulting distribution in parameter space represents an estimate for the probability distribution of the parameters and thus allows us to calculate the confidence levels for the parameters assuming that the values follow a normal distribution (simulated annealing; e.g. Pawellek 2017).

### 3.2 Stars with IR excess

We identified nine out of 12 stars (75 per cent) that show infrared excess and therefore suggest the presence of a debris disc. Since we cannot draw strong conclusions on HD 173167 (see Section 3.3), we might even say that nine out of 11 systems ( $\sim 82$  per cent) possess debris discs. A comparable, high detection rate of 6/9 F stars for the BPMG was noted in Churcher et al. (2011). As noted in the introduction, this is in contrast to the results of studies that find a typical occurrence rate for debris discs of  $\sim 20$  per cent around FGK-stars for volume-limited samples with older mean ages around Gyr (e.g. Su et al. 2006; Eiroa et al. 2013; Chen et al. 2014; Marshall et al. 2016; Sibthorpe et al. 2018).

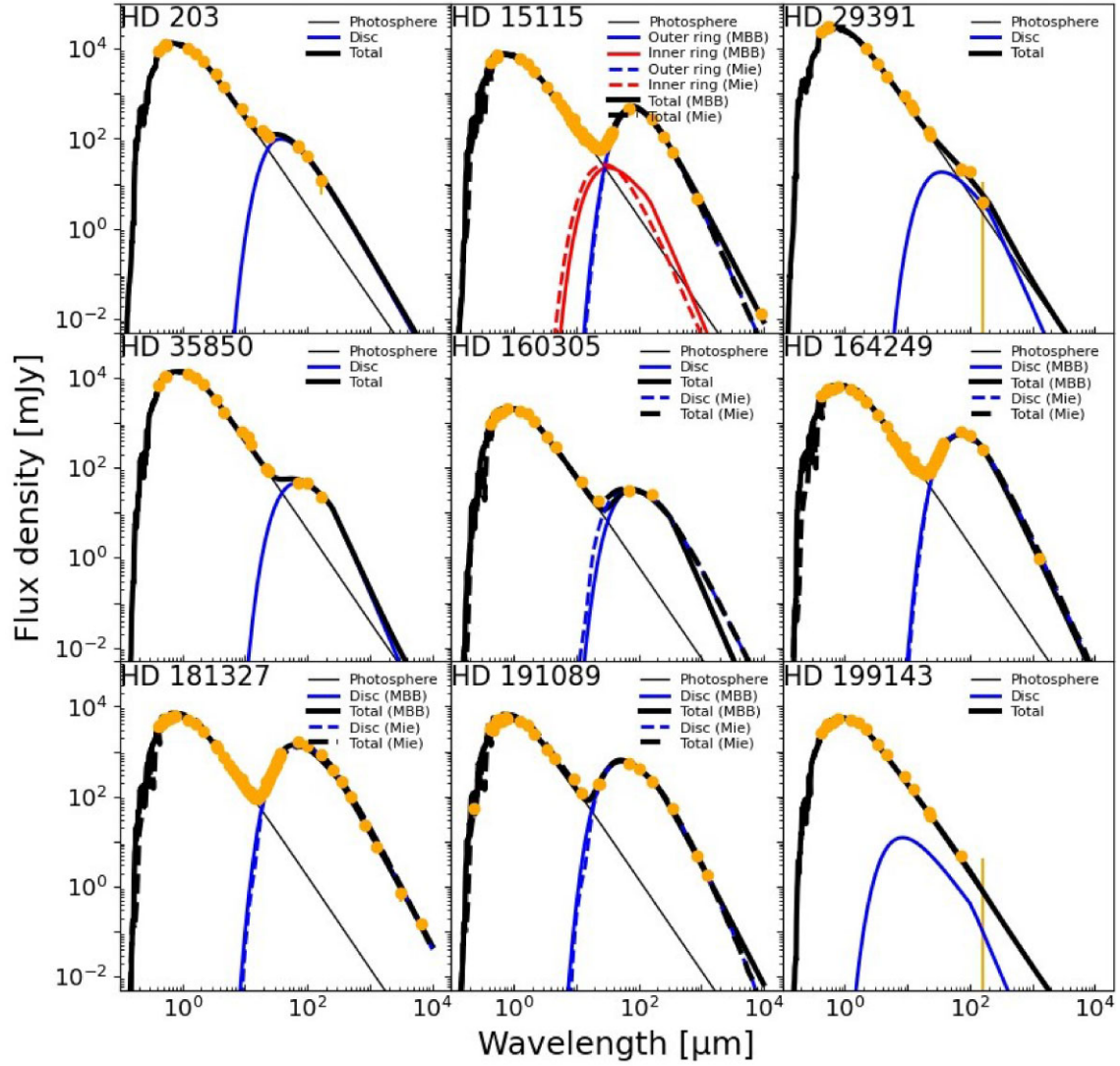


**Figure 1.** SEDs for the debris discs detected around F stars in the BPMG. Solid lines show the modified blackbody fit. For spatially resolved targets, dashed lines show the size distribution fit using Mie theory. Blue lines represent the outer ring and red lines the inner ring (if present). For the SED of HD 15115, both disc components were fitted with a modified blackbody model (solid line) and a size distribution model (dashed line).

**Table 3.** SED fitting results.

HD	Resolved	Modified blackbody model					Grain-size distribution model					
		$f_d$ ( $10^{-5}$ )	$T_{\text{bb}}$ (K)	$R_{\text{bb}}$ (au)	$R_{\text{est, sub-mm}}$ (au)	$R_{\text{sub-mm}}$ (au)	$s_{\text{blow}}$ ( $\mu\text{m}$ )	$s_{\text{min}}$ ( $\mu\text{m}$ )	$s_{\text{min}}/s_{\text{blow}}$	$q_{\text{SED}}$	$T_{\text{dust}}$ (K)	$f_d$ ( $10^{-5}$ )
203	No	15	134 $\pm$ 4	8.3 $\pm$ 1.5	30 $\pm$ 8	—	1.18	—	—	—	—	—
14082A	—	—	—	—	—	—	0.87	—	—	—	—	—
15115	Yes	51	62 $\pm$ 1	38 $\pm$ 7	129 $\pm$ 27	93 $\pm$ 21	0.91	4.6 $\pm$ 0.2	5.1 $\pm$ 0.2	3.84 $\pm$ 0.06	61.4 $\pm$ 1.9	60.0
29391	No	0.5	101 $\pm$ 20	18 $\pm$ 5	21 $\pm$ 9	—	1.81	—	—	—	—	—
35850	No	4.0	74 $\pm$ 4	19 $\pm$ 8	54 $\pm$ 6	—	0.51	—	—	—	—	—
160305	Yes	14	56 $\pm$ 10	32 $\pm$ 9	71 $\pm$ 23	88 $\pm$ 2	0.67	0.6 $\pm$ 0.6	0.9 $\pm$ 0.8	3.5 <sup>a</sup>	77.4 $\pm$ 14.5	22.4
164249	Yes	88	60 $\pm$ 1	39 $\pm$ 8	93 $\pm$ 15	63 $\pm$ 24	0.89	2.8 $\pm$ 0.1	3.2 $\pm$ 0.2	3.73 $\pm$ 0.05	77.4 $\pm$ 2.6	94.2
173167	—	—	—	—	—	—	0.85	—	—	—	—	—
181327	Yes	264	78 $\pm$ 1	22 $\pm$ 4	125 $\pm$ 22	81 $\pm$ 16	1.02	1.1 $\pm$ 0.2	1.1 $\pm$ 0.2	3.45 $\pm$ 0.05	61.4 $\pm$ 4.7	227
191089	Yes	151	92 $\pm$ 1	15 $\pm$ 3	37 $\pm$ 4	45 $\pm$ 16	0.98	1.2 $\pm$ 0.3	1.2 $\pm$ 0.3	3.43 $\pm$ 0.08	83.6 $\pm$ 4.9	118
199143	No	47	1000 $\pm$ 100	0.2 $\pm$ 0.1	0.8 $\pm$ 0.3	—	0.74	—	—	—	—	—
213429	—	—	—	—	—	—	0.74	—	—	—	—	—

*Note.* The blow-out limit is calculated assuming Mie theory and pure astronomical silicate (Draine 2003) with a bulk density of  $3.3 \text{ g/cm}^3$ . The estimated disc radius seen at sub-mm wavelengths,  $R_{\text{est, sub-mm}}$ , is calculated by equation (2) using the parameters inferred in this work. A grain-size distribution fit is done if the disc is spatially resolved. <sup>a</sup> The parameter  $q_{\text{SED}}$  was fixed due to a lack of photometric data in the far-infrared. Only HD 15115 shows evidence for a warm disc component.



The fractional luminosities of the excess emission lie between  $1.2 \times 10^{-5}$  and  $4.1 \times 10^{-3}$ , which are typical values for debris discs (e.g. Eiroa et al. 2013; Chen et al. 2014; Holland et al. 2017; Sibthorpe et al. 2018). The inferred blackbody temperatures lie between 51 and 600 K corresponding to blackbody radii between 0.3 and 52 au.

Pawellek & Krivov (2015) found a relation between the ratio of the spatially resolved disc radius seen at FIR wavelengths to blackbody radius and the stellar luminosity of the form

$$\frac{R_{\text{FIR}}}{R_{\text{BB}}} = A \left( \frac{L}{L_{\text{sun}}} \right)^B. \quad (2)$$

The disc radius seen at FIR wavelengths in this relation is that inferred from resolved *Herschel*/PACS imaging and the blackbody radius that of a fit to the spectrum that is comparable with the modified blackbody fit used here. We use the updated values of  $A$  and  $B$  from Pawellek (2017) with  $A = 6.49 \pm 0.86$  and  $B = -0.37 \pm 0.05$  assuming pure astronomical silicate (Draine 2003) for the dust material.

Estimates of the FIR radii of the discs using equation (2) give values between 1.5 and 215 au which are  $\sim 4$  times larger than  $R_{\text{BB}}$ . In Section 4.4, we compare those estimates to the observed disc radii of the spatially resolved discs.

### 3.3 Notes for particular targets

**HD 14082A:** For HD 14082A all WISE bands (3.4, 4.6, 12, and 22  $\mu\text{m}$ , see WISE All-Sky Catalog, Wright et al. 2010) and Spitzer/MIPS (24  $\mu\text{m}$ , Chen et al. 2014) exhibit significant excess emission, but no excess was found with Spitzer/MIPS (70  $\mu\text{m}$ ) or *Herschel*/PACS. The star forms a binary system (Mamajek & Bell 2014; Elliott & Bayo 2016) with its companion (HD 14082B) known to exhibit IR excess in the mid- and far-infrared (e.g. Riviere-Marichalar et al. 2014). After checking the WISE and MIPS data, we found the photometry to be confused in all bands since those instruments were not able to differentiate between the two stellar components. Thus, we assume no significant excess emission for HD 14082A while the excess found around HD 14082B is real.

**HD 29391:** The star HD 29391 (51 Eri) shows significant excess at MIPS24, MIPS70, and PACS100 providing a good constraint on the disc as noted previously (Riviere-Marichalar et al. 2014). The target possesses the only planetary companion detected in our sample (see Section 2.3). The planet's separation is  $\sim 13$  au. With the disc's  $R_{\text{BB}} = 9 \pm 2$  au and an estimated FIR radius of  $R_{\text{FIR}} = 30.7 \pm 13.4$  au, we assume the planet to be located closer to the star than the planetesimal belt.

**HD 173167:** The star HD 173167 possesses only photometric data up to 22  $\mu\text{m}$  so that we cannot draw any conclusions about a possible FIR excess. However, the mid-infrared data do not reveal significant excess.

**HD 199143:** Considering HD 199143, there are mid-infrared data available as well as data from *Herschel*/PACS. The excess emission is significant only for the MIPS24 band, but WISE data also show a marginal detection of excess emission at 22  $\mu\text{m}$ . Despite the presence of a close binary companion, we could rule out confusion issues since the companion is several orders of magnitude fainter than the primary. Therefore, we assume that we detect emission from hot dust close to the star. In our sample, this is the only target with a close-in disc, with a dust temperature of 600 K and a blackbody radius of 0.3 au. The FIR radius is estimated to be 1.5 au.

While Table 2 gives the significance of the excess at 24  $\mu\text{m}$  as  $7\sigma$ , this might be overestimated because of the SED fit being to both star and disc. Fitting the star without including the disc component results in a 24- $\mu\text{m}$  excess of  $3\sigma$ . Thus, the excess is real, albeit at low significance.

### 3.4 IR excess in multiple systems

We found that all four stars in our sample without a known stellar companion possess a debris disc (HD 203, HD 15115, HD 160305, and HD 191089). Furthermore, three out of the five systems with companions at projected separations larger than 135 au (HD 14082A, HD 29391, HD 164249, HD 173167, and HD 181327) harbour a disc as well. Two systems have companions at projected separations below 25 au where one shows evidence of debris. (HD 35850 has debris and a companion at a distance of 0.021 au, while HD 213429 has no debris and a companion with an estimated separation of  $\sim 2$  au). Only HD 199143 has a stellar companion at an intermediate separation of  $\sim 50$  au (in addition to a wide separation component at  $\sim 15\,000$  au, Tokovinin 1997; Mamajek & Bell 2014). Significant mid-infrared excess (see Section 3.3) hints at the presence of a close-in debris disc with  $R_{\text{BB}} = 0.3$  au.

These results are broadly consistent with those of Yelverton et al. (2019). That study analysed a sample of 341 multiple systems and found that for binary stars with separations between  $\sim 25$  and 135 au, no discs could be detected. Since these values are comparable to typical debris disc radii (e.g. Booth et al. 2013; Pawellek et al. 2014; Matrà et al. 2018), it was suggested that the binaries are clearing the primordial circumstellar or circumbinary material via dynamical perturbation. While the detection rates for separations larger than 135 au were found to be similar to the rates for single stars (at  $\sim 20$  per cent), only  $\sim 8$  per cent of binary systems with separations below 25 au showed evidence for debris.

Thus, considering the three aforementioned targets (HD 35850, HD 199143, and HD 213429), we would expect a lower number of disc detections for these systems, but as they are only three in number, we cannot draw any conclusions about detection rates.

## 4 DISC IMAGING

Different observational wavelengths are sensitive to different sizes of dust grains. While the emission seen by (sub-)mm telescopes such as ALMA is expected to be dominated by thermal emission from mm-size particles, near-infrared instruments such as VLT/SPHERE (Beuzit et al. 2019) are expected to trace scattered light from micron-size grains. Particles as small as micron-size are significantly affected by radiation pressure and other transport processes (e.g. Burns, Lamy & Soter 1979) so that their distribution is expected to extend far beyond their birth environment. In contrast, the large mm-size grains are expected to stay close to the parent belt. Hence, the disc size inferred in sub-mm observations is the best tracer of the location of a system's planetesimal belt, which might differ from the radial extent seen in near-infrared scattered light. Nevertheless, such short wavelength observations can also be modelled to infer the planetesimal belt location, and comparing the disc structure seen at different wavelengths provides information on the physical mechanisms shaping debris discs.

### 4.1 ALMA reduction procedure

Atacama Large Millimeter/submillimeter Array observations of six out of the 12 stars in our sample were retrieved from the ALMA

**Table 4.** BPMG F stars ALMA observations summary.

Target	Date dd-mm-yyyy	Project ID	Band	Continuum rms $\mu\text{Jy beam}^{-1}$	Continuum beam size	Cont. image weighting	Original reference for data set
HD14082A	31-08-2015	2013.1.01147	6	150 <sup>a</sup>	$1''.8 \times 1''.6$	Natural	This work
HD15115	01-01-2016	2015.1.00633	6	15	$0''.6 \times 0''.6$	Briggs 0.5	MacGregor et al. (2019)
	09-06-2016	2015.1.00633	6				MacGregor et al. (2019)
HD29391	13-10-2016	2016.1.00358	6	23	$0''.2 \times 0''.2$	Natural	Pérez et al. (2019)
HD164249	10-03-2014	2012.1.00437	6	45	$1''.1 \times 1''.0$	0''.7 Taper	This work
	11-08-2015	2013.1.01147	6				This work
HD181327	25-07-2016	2015.1.00032	7	27	$0''.2 \times 0''.2$	Natural	This work
HD191089	23-03-2014	2012.1.00437	6	12	$0''.9 \times 0''.6$	Briggs 0.0	This work
	30-05-2018	2017.1.00704	6				Kral et al. (2020)
	14-09-2018	2017.1.00200	6				Matrà et al. (in preparation)

<sup>a</sup>At field centre. HD14082A is, however,  $\sim 14''$  from field centre, where the primary beam level drops to 46%. The sensitivity per beam at that location would be  $326 \mu\text{Jy beam}^{-1}$ . rms noise levels, beam sizes, and weightings of multiple data sets refer to imaging of the joint data sets.

archive. Three of the analysed data sets have already been presented in literature work (HD 15115, HD 29391, and HD 191089, MacGregor et al. 2019; Pérez et al. 2019; Kral et al. 2020) but are re-analysed here to maintain consistency across the sample. We also present the first ALMA image of HD 164249 and new images of the disc around HD 181327. For the latter target another data set was published by Marino et al. (2016), but due to their lower resolution, we do not use those data here. In addition to that, we present new constraints for HD 14082A for which dust emission was not detected (as was also the case for HD 29391).

The targets were observed as single pointings with the ALMA 12-m array within the context of a variety of projects, over different ALMA Cycles, leading to inhomogeneous sensitivities, resolutions, and wavelengths (see Table 4). For each target, and each observing date, we carried out standard calibration steps to obtain calibrated visibility data sets; we used the same CASA and pipeline version as used in the original reduction delivered by the ALMA observatory.

Later processing was carried out homogeneously in CASA v5.4.0. If available, for each target, we concatenated multiple data sets at similar frequencies to obtain a final combined visibility data set. We also averaged in time (to 30-s integrations) and frequency (to 2-GHz-wide channels) to reduce the size of each data set and speed up imaging and modelling.

We then carried out continuum imaging using the CLEAN algorithm implemented through the *tclean* CASA task. We used multiscale deconvolution (Cornwell 2008) in multifrequency synthesis mode, adapting the choice of visibility weighting and/or tapering schemes to achieve a good trade-off between image sensitivity and resolution. The weighting choices, rms noise levels (measured in image regions free of source emission), and synthesized beam sizes achieved are listed in Table 4.

Discs are detected and resolved around four out of the six BPMG F stars with existing ALMA observations. Fig. 2 shows the ALMA images for the resolved discs, as well as the best-fitting models, residuals, and deprojected visibilities. No detection was achieved near the location of HD 14082A and HD 29391 in the respective images. We conservatively derive  $3\sigma$  upper limits of  $<5.8$  and  $<3.5$  mJy for the flux density of the two belts, respectively, by spatially integrating emission within a  $5''$  radius circular region centred on the expected stellar location. The high values for the upper limits are caused by the relatively small beam used for the observation of HD 29391 and the fact that HD 14082A is significantly offset from the phase centre, increasing the already high rms of that observation.

For both targets, no (sub-)mm observations were reported in the literature before.

For the visibility modelling, we follow the method described, e.g. in Matrà et al. (2019), using RADMC-3D<sup>1</sup> to calculate model images from a given density distribution, which we here assume to be a radial and vertical Gaussian described by

$$\rho = \Sigma_0 e^{-\frac{(r-r_c)^2}{2\sigma^2}} e^{-\frac{z^2}{2(hr)^2}} \frac{1}{\sqrt{2\pi}hr}, \quad (3)$$

with symbols having the same meaning as in equation (1) of (Matrà et al. 2018). The vertical aspect ratio  $h = H/R$  is radially constant and fixed to 0.03 for belts that are too face-on or too low S/N for it to be meaningfully constrained. Additionally, rather than fitting for the normalization factor  $\Sigma_0$ , we fit for the total flux density of the belt in the model images. When calculating model images, we also assume the grains to act as blackbodies and therefore to have a temperature scaling as  $r^{-0.5}$ .

After producing a model image, we Fourier transform it and sample the model visibility function at the same  $u$ - $v$  locations as the data using the GALARIO software package (Tazzari, Beaujean & Testi 2018). This produces model visibilities that can be directly compared with the observed ones. This process is then used to fit the model to the data through a Markov Chain Monte Carlo implemented using the EMCEE v3 software package (Foreman-Mackey et al. 2013, 2019). This samples the posterior probability function of the  $n$ -dimensional parameter space of our model using the affine-invariant sampler of Goodman & Weare (2010). We use a likelihood function  $\propto e^{-\chi^2}$  and uniform priors on all model parameters. In addition to the model parameters entering the equation describing the density distribution, we fit for RA and Dec offsets of the belt's geometric centre from the phase centre of the observations and for a weight-rescaling factor to account for the inaccurate data weights (and hence uncertainties) typically delivered by ALMA (e.g. Marino et al. 2018; Matrà et al. 2019). We fit these additional, nuisance parameters separately to each observing date for any given target.

Table 5 shows best-fitting parameters and uncertainties derived for each of the resolved belts, taken as the  $50^{+34}_{-34}$ th percentiles of the marginalized posterior probability distribution of each parameter.

<sup>1</sup><http://www.ita.uni-heidelberg.de/~dullemond/software/radmc-3d/> (by C. Dullemond, A. Juhasz, A. Pohl, F. Sereshti, R. Shetty, T. Peters, B. Commerçon and M. Flock).

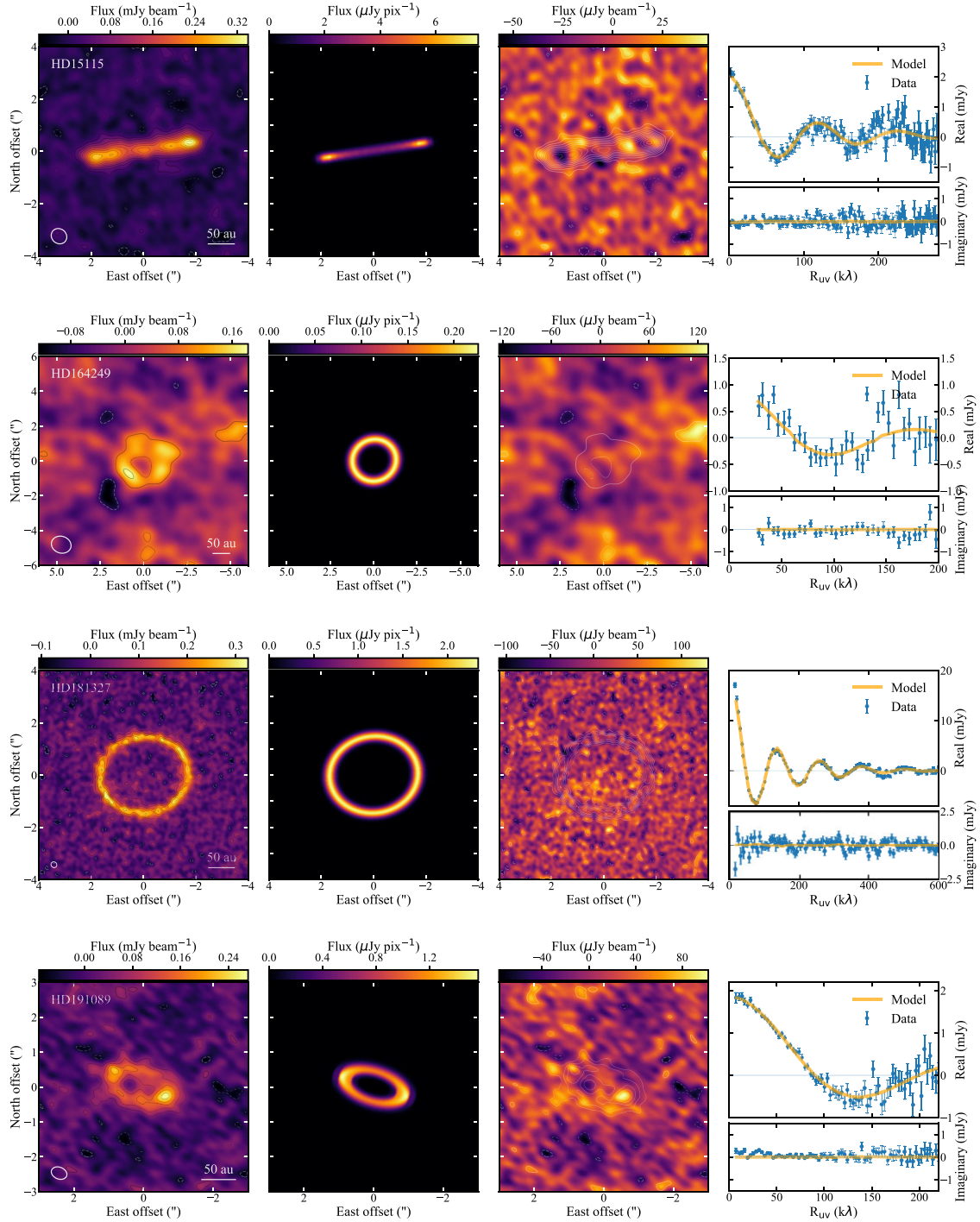


**Figure 2.** ALMA models for four resolved debris discs. From top to bottom: HD 15115, HD 164249, HD 181327, and HD 191089.

Fig. 2 shows full-resolution model images and residuals obtained by subtracting the best-fitting visibility model from the data and imaging without CLEAN deconvolution. The residual images look mostly consistent with noise, indicating that our models provide a very good fit to the data. However, we note that some residual, extended emission is detected (1) interior to the HD 181327 ring, to the SE of the star, and (2) at the SW ansa, and along the S side of the HD 191089 belt. While this could be due to true substructure in the dust morphology of these systems, this does not significantly affect the measurement of the radius of

the bulk of the planetesimal belt material, which we are most interested in.

## 4.2 ALMA results

### 4.2.1 A newly resolved disc around HD 164249

The disc around HD 164249 was observed with ALMA at 1.35 mm and is spatially resolved for the first time increasing the number of resolved debris discs reported in the literature to 153 according to the



**Table 5.** Resolved discs and fitting parameters for ALMA models.

HD	$\lambda$ ( $\mu\text{m}$ )	$F_{\nu_*}$ ( $\mu\text{Jy}$ )	$F_{\text{belt}}$ (mJy)	$R$ (au)	$\Delta R$ (au)	$h$	$i$ ( $^\circ$ )	PA ( $^\circ$ )	$\Delta\text{RA}$ ( $''$ )	$\Delta\text{Dec}$ ( $''$ )
15115	1340	$^{43+20}_{-20}$	$2.02^{+0.06}_{-0.06}$	$93.4^{+1.0}_{-1.3}$	$^{21+6}_{-7}$	$^{0.051^{+0.012}_{-0.016}}$	$^{87.8^{+1.4}_{-1.3}}$	$98.5^{+0.3}_{-0.3}$	$0.08^{+0.03}_{-0.03}$	$-0.04^{+0.01}_{-0.01}$
164249	1350	—	$0.96^{+0.14}_{-0.13}$	$63^{+4}_{-3}$	$^{24^{+11}_{-11}}$	—	$<49$	$^{113}$	$-0.08^{+0.08}_{-0.09}$	$-0.17^{+0.08}_{-0.08}$
*181327	880	$^{39+25}_{-21}$	$18.8^{+0.3}_{-0.3}$	$81.3^{+0.3}_{-0.3}$	$16.0^{+0.5}_{-0.6}$	$<0.09$	$30.0^{+0.5}_{-0.5}$	$97.8^{+1.0}_{-1.0}$	$-0.005^{+0.005}_{-0.005}$	$-0.028^{+0.004}_{-0.004}$
*191089	1270	$^{45+21}_{-21}$	$1.83^{+0.03}_{-0.03}$	$44.8^{+0.9}_{-0.9}$	$16^{+3}_{-3}$	$^{0.10^{+0.04}_{-0.05}}$	$60^{+1}_{-1}$	$73^{+1}_{-1}$	$^{0.032^{+0.012}_{-0.012}}$	$^{d-0.012^{+0.008}_{-0.008}}$

Note. \*The model fit leaves significant residuals. <sup>a</sup> Marginally resolved/detected, i.e. having a posterior probability distribution with a non-zero peak but consistent with zero at the  $3\sigma$  level. <sup>b</sup> Inclination consistent with  $90^\circ$  (perfectly edge-on) at the  $3\sigma$  level. <sup>c</sup> Quantity unconstrained at the  $3\sigma$  level, but with a pronounced peak at the median value reported. <sup>d</sup> Offsets refer to 2018 data set. For 2014 data set, offsets were  $\Delta\text{RA} = 0.12^{+0.04}_{-0.04}$  and  $\Delta\text{Dec} = 0.02^{+0.02}_{-0.02}$ .

data base for resolved discs.<sup>2</sup> It shows a face-on orientation with an inclination below  $49^\circ$ . The planetesimal belt is found at 63 au with a disc width of 24 au using a Gaussian disc model. The disc was not resolved at any other wavelength before.

#### 4.2.2 Previously resolved discs

We re-analysed the data sets of two targets (HD 15115, HD 191089) presented in former studies to infer the system parameters, such as the disc radius, in a consistent way and present the results of new high-resolution data for HD 181327.

**HD 15115:** We find the edge-on disc of HD 15115 with an inclination of  $88^\circ$  to be located at  $93.4^{+1.0}_{-1.3}$  au with a disc width of  $21^{+6}_{-7}$  au using a Gaussian ring model. The results from MacGregor et al. (2015) and MacGregor et al. (2019), which are based on the same data set as our study, suggest the disc to extend from 44 to 92 au with a 14 au wide gap at 59 au. MacGregor et al. (2019) suggest that a planet with a mass of  $0.16 M_{\text{Jup}}$  is creating this gap, but so far no planet could be detected (see Section 2.3). Our results do not show evidence for a gap in the disc, which may be because of the different parametrizations of the two models; MacGregor et al. (2019) assume a two-dimensional (2D) disc model using a power law for the radial surface density distribution and an infinitesimally small vertical scale height, whereas our disc model assumes Gaussian radial and vertical density distributions (the latter was found to be marginally resolved in our analysis).

**HD 181327:** The face-on disc around HD 181327 was inferred to have a radius of  $81.3 \pm 0.3$  au and width of  $16^{+0.5}_{-0.6}$  au using a Gaussian ring model. This is comparable with the 86 au radius and width of 23 au found by Marino et al. (2016) from lower resolution ALMA Band 6 data.

**HD 191089:** The debris disc around HD 191089 was observed at 1.27 mm and formerly presented in Kral et al. (2020), which reported a disc ring at  $43.4 \pm 2.9$  au with a width of  $<22.5$  au and an inclination of  $\sim 52^\circ$ . With our Gaussian ring model, we inferred an inclination of  $60^\circ$  and a disc radius of  $44.8 \pm 0.9$  au with a width of  $16 \pm 3$  au. The scale height was constrained to be smaller than 0.1 at a  $3\sigma$  significance. We note that our data set does contain not only the data used in Kral et al. (2020) but also a combination of those with data from the ‘Resolved ALMA and SMA Observations of Nearby Stars’ (REASONS) programme (Sepulveda et al. 2019), which have a higher spatial resolution, as well as older observations from 2012 (see Table 4).

#### 4.2.3 Gas emission

We visually checked the data cubes of the four ALMA-resolved targets for CO gas emission but did not detect any. HD 181327 is the only target in our sample of F stars in the BMPG with a gas detection presented in Marino et al. (2016). That study found a significant amount of  $^{12}\text{CO}$  in its disc based on the  $J = 2 - 1$  excitation level and inferred a total CO-gas mass of  $1.2 \dots 2.9 \times 10^{-6} M_{\oplus}$ . The gas is consistent with a secondary origin if the planetesimals in the disc around HD 181327 possess a similar volatile fraction compared to Solar system comets. Our observations included the  $J = 3 - 2$  excitation level. The non-detection could be consistent with the  $J = 2 - 1$  detection depending on excitation conditions, but a full gas analysis, including optimizing detection, and considering the wide range of possible excitation conditions is needed to draw a definitive conclusion.

### 4.3 Imaging at other wavelengths

#### 4.3.1 Scattered light and MIR observations

Scattered light observations give us an additional opportunity to estimate the planetesimal belt radii of discs especially if they were not observed in thermal emission. Furthermore, observations at wavelengths shorter than sub-mm trace dust grain sizes smaller than those seen with ALMA and thus can help to investigate transport processes within the discs. While most of the spatially resolved discs in the BMPG were observed with ALMA, there is one disc (HD 160305) observed only in scattered light.

**HD 160305:** The disc around HD 160305 was recently detected with VLT/SPHERE by Perrot et al. (2019) in scattered light. The debris dust is confined to a narrow ring between 86 and 90 au. It shows a near edge-on inclination and a brightness asymmetry between its western and eastern side. Perrot et al. (2019) suggest different scenarios as the reason for this asymmetry, such as strong recent collisions of planetesimals, interactions with massive companions, or pericentre glow effects, but are not able to differentiate between these scenarios.

**HD 15115:** Scattered light observations of HD 15115 (e.g. Kalas, Fitzgerald & Graham 2007; Engler et al. 2019) revealed a strong asymmetry of the disc, which is not seen in ALMA observations. Kalas et al. (2007) report a disc extent up to 580 au on the west side and 340 au on the east side. MacGregor et al. (2019) concluded that the mechanism causing the asymmetry is affecting only the smallest grains, suggesting interaction with the local interstellar medium (ISM) as a likely reason for it. Engler et al. (2019) derived the maximum of polarized flux density at a location of  $94 \pm 2$  au, which is assumed to correspond to the location of the planetesimal belt (similar to the radius we find in Table 5).

<sup>2</sup><https://www.astro.uni-jena.de/index.php/theory/catalog-of-resolved-disks.html> (by N. Pawellek & A. Krivov)



**Table 6.** Discs resolved with *Herschel*/PACS.

HD	$R_{\text{in}}$ (au)	$R_{\text{out}}$ (au)	$R_{\text{FIR}}$ (au)	$\Delta R_{\text{FIR}}$ (au)	$i$ ( $^{\circ}$ )	PA ( $^{\circ}$ )
15115	$40.6 \pm 23.7$	$145.4 \pm 29.0$	$93.0 \pm 18.7$	$52.4 \pm 18.7$	$85.9 \pm 3.7$	$98.9 \pm 2.4$
164249	$13.3 \pm 11.5$	$43.0 \pm 21.2$	$28.2 \pm 12.0$	$14.8 \pm 12.0$	$68.1 \pm 20.8$	$175.1 \pm 66.5$
181327	$25.7 \pm 25.5$	$134.4 \pm 30.8$	$80.0 \pm 20.0$	$54.3 \pm 20.0$	$30.1 \pm 8.9$	$101.6 \pm 11.6$

*Note.*  $R_{\text{in}}$  and  $R_{\text{out}}$  give the inner and outer radii for *Herschel*/PACS inferred with the method described in Section 4.3.2 following the procedure of Yelverton et al. (2019) and Xuan et al. (2020).  $R_{\text{FIR}}$  is the central radius defined as  $R_{\text{FIR}} = 0.5 \times (R_{\text{in}} + R_{\text{out}})$ ,  $\Delta R_{\text{FIR}}$  gives the disc width. The parameters  $i$  and PA give the inclination and position angle.

**HD 181327:** *HST*/NICMOS observations of HD 181327 in scattered light presented by Schneider et al. (2006) derived a disc radius of 86 au with a width of 36 au. While the radius is in agreement with our ALMA-based results, the disc width is broader in scattered light than at sub-mm wavelengths. We would expect a broader disc at shorter wavelengths since such observations trace smaller particles that are more susceptible to transport processes. Asymmetries were reported by Stark et al. (2014), which suggested a recent catastrophic disruption or a warping of the disc by the ISM as probable causes.

**HD 191089:** Churcher et al. (2011) observed HD 191089 at  $18.3 \mu\text{m}$  with T-ReCS on Gemini South and found excess emission between 28 and 90 au. This is in agreement with the belt location inferred from observations of the HD 191089 disc performed by *HST*/NICMOS and STIS and *Gemini*/GPI (Ren et al. 2019). That study detected scattered light between 26 and 78 au. In addition to the dust ring, a halo was found extending to  $\sim 640$  au, but no brightness asymmetries were identified. However, similar to HD 181327, the disc is broader in scattered light than at mm wavelengths.

#### 4.3.2 FIR observations with *Herschel*/PACS

Three discs in the BPMG sample were spatially resolved in the FIR with *Herschel*/PACS (HD 15115, HD 164249, and HD 181327). To infer their radii in a homogeneous way, we apply the method described in Yelverton et al. (2019) and Xuan et al. (2020). The Point Spread Function (PSF) of the star is derived from observations of the *Herschel* calibration star HD 164058 and then rotated to the appropriate orientation and scaled to the stellar flux derived from the SED. Then we generate an axisymmetric, optically thin disc model and assume that the surface brightness is proportional to  $r^{-1.5}$  with  $r$  being the distance to the star. The dust temperature at a distance  $r$  is assumed to follow  $r^{-0.5}$  as for blackbody grains. The free parameters of the model are the total disc flux density, the inner and outer edges of the disc,  $R_{\text{in}}$  and  $R_{\text{out}}$ , inclination, and position angle. We also include a 2D offset to account for non-perfect *Herschel* pointing. The model disc is convolved with the PSF and then compared to the *Herschel*/PACS image by calculating the goodness of fit,  $\chi^2$ . We estimate the parameters using the EMCEE package. To get disc radii to be compared with those inferred from ALMA images that assumed a Gaussian radial profile, we derive a radius from *Herschel*/PACS,  $R_{\text{FIR}} = 0.5 \times (R_{\text{in}} + R_{\text{out}})$ . We note that in some cases, the inner and outer edge of a disc might be poorly constrained, and in any case,  $R_{\text{FIR}}$  could differ from the location of the peak of the surface brightness that would have been inferred if observed at higher spatial resolution.

The modelling results of the *Herschel*/PACS images for the BPMG sample are listed in Table 6. In all cases, the inclination and position angle are in agreement with ALMA observations listed in Table 5. For HD 15115 and HD 181327, the radii,  $R_{\text{FIR}}$ , are in agreement with values inferred from ALMA observations but possess uncertainties of up to 25 percent. The disc widths seem to

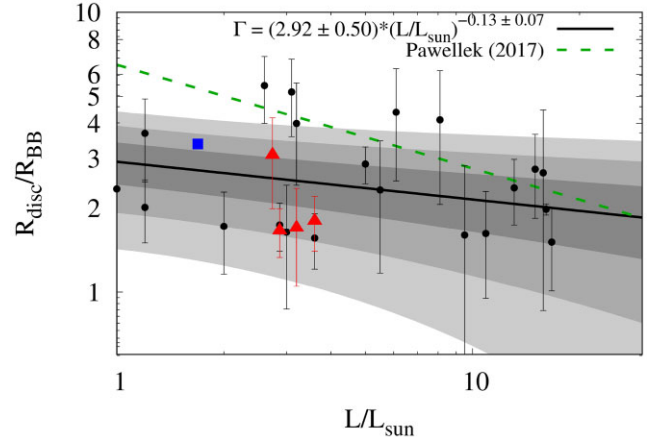


**Figure 3.** Spatially resolved disc radius-to-blackbody radius ratio as a function of stellar luminosity for NIR, FIR, and sub-mm wavelengths. Black circles show the ALMA sample from Matrà et al. (2018), red asterisks show the ALMA-resolved F stars, and the blue square the SPHERE-resolved F-star HD 160305. The grey shaded areas depict the 1, 2, and  $3\sigma$  levels of the correlation. The green dashed line shows the trend found in Pawellek (2017) from the *Herschel*-resolved disc radius.

be larger compared to ALMA but show only deviations within  $2\sigma$  so that we assume the discs to be similar in ALMA and *Herschel*. A broader extent in *Herschel* might indicate the presence of transport mechanisms altering the orbits of smaller dust particles towards larger eccentricities. For HD 164249, the *Herschel* results show large uncertainties due to the low spatial resolution. The *Herschel* radius is a factor of 2.2 smaller than that from ALMA; however, the two radii are not significantly different ( $\sim 2\sigma$ ) and the higher resolution ALMA result is a better estimate of the planetesimal belt location.

#### 4.4 Ratio of spatially resolved disc radius to blackbody radius

We calculate the ratio of sub-mm radius to blackbody radius for the four ALMA-resolved discs in our sample. In addition, we infer the ratio of the scattered light radius to blackbody radius for HD 160305. Given the knowledge that there is a potential trend in sub-mm disc sizes with stellar luminosity (Matrà et al. 2018), and also a trend in the FIR size to blackbody radius ratio with stellar luminosity (Booth et al. 2013; Pawellek & Krivov 2015), we compare the five discs to a sample of ALMA-resolved discs with a broader stellar luminosity range (Matrà et al. 2018). In Fig. 3, we plot the radius ratio as a function of stellar luminosity. The actual disc width inferred by ALMA observations (see Table 5) is given by the error bars.

For our sample of F stars, the values of this ratio lie between 1.6 and 3.4 where the system with the lowest stellar luminosity (HD 160305) possesses the highest value. Including the ALMA sample of Matrà et al. (2018) and fitting a trend of the form in equation 2 for how

the ratio depends on stellar luminosity, we infer a slight decrease of the ratio with stellar luminosity finding parameter values of  $A = 2.92 \pm 0.50$  and  $B = -0.13 \pm 0.07$ .

This result is different from the trend presented in Pawellek & Krivov (2015) and Pawellek (2017) based on disc sizes from *Herschel* images, which showed parameter values of  $A = 6.49 \pm 0.86$  and  $B = -0.37 \pm 0.05$  (see green dashed line in Fig. 3). For systems with stellar luminosities larger than  $5L_{\text{sun}}$ , the radius ratio of the ALMA sample is in agreement with Pawellek & Krivov (2015). The different fit is caused by a number of systems with lower luminosities including our sample of ALMA-resolved F stars that show relatively small ratios. Possible reasons for the different trends could be that *Herschel* had a lower resolution and so there may be systematic uncertainties in the derived disc radii, or the discs could be larger when traced in the far-IR due to such wavelengths tracing small dust in the halo that extends beyond the planetesimal belt. However, our analysis of the *Herschel* images of the BPMG F stars in Section 4.3.2 inferred radii that are consistent with those from ALMA images. Considering Pawellek & Krivov (2015), none of the BPMG targets was used to derive the radius ratio versus luminosity trend, but the study inferred radii between 93 and 112 au for HD 181327 depending on the dust composition assumed, which is in agreement with the results of ALMA and *Herschel*. A more detailed analysis is needed to investigate possible causes for the different outcomes between the *Herschel* and ALMA samples. A systematic difference might indicate the presence of dynamical processes affecting the size distribution in a way not considered before.

## 5 SED MODELLING REVISITED

As mentioned before, five discs of our sample were spatially resolved (four with ALMA and one with SPHERE, see Table 5). This allows us to apply a more detailed model to fit the SEDs of these five discs rather than using a simple modified blackbody model as in Section 3. In the following approach, we model the dust-size distribution and composition.

### 5.1 Modelling approach

We use the SONATA code (Pawellek et al. 2014; Pawellek & Krivov 2015) and apply the same PHOENIX-GAIA stellar photospheric models (Brott & Hauschildt 2005) to determine the host star contribution in a similar approach as for the modified blackbody fits (MBB, see Section 3). While for the MBB model we simply fitted a dust temperature and a fractional luminosity without consideration of dust properties, the SONATA code calculates the temperature and the thermal emission of dust particles at different distances to the star. It assumes compact spherical grains and uses Mie theory to derive the absorption efficiencies (Bohren & Huffman 1983). The dust composition is assumed to be pure astronomical silicate (Draine 2003) with a bulk density of  $3.3 \text{ g/cm}^3$ . The code sums up the emission of particles within a range of sizes to generate the SED. The flux densities given for wavelengths shorter than  $5 \mu\text{m}$  are not used to fit the dust disc since in this wavelength regime the stellar photosphere rather than the dust dominates the emission.

We apply a power law for the size distribution and assume a Gaussian radial distribution of the dust using the surface number density  $N(r, s)$ :

$$N_{\text{SED}}(r, s) \sim s^{-q_{\text{SED}}} \frac{1}{\sqrt{2\pi} \Delta R_{\text{disc}}} \exp \left[ -\frac{1}{2} \left( \frac{r - R_{\text{disc}}}{\Delta R_{\text{disc}}} \right)^2 \right]. \quad (4)$$

Here,  $r$  represents the distance to the star,  $R_{\text{disc}}$  the peak, and  $\Delta R_{\text{disc}}$  the width of the radial distribution. The parameter  $s$  is the grain radius and  $q_{\text{SED}}$  is the SED power-law index for the size distribution. The surface number density is directly connected to the surface density,  $\Sigma$ , by  $\Sigma(r, s) ds = \pi s^2 N(r, s) ds$ .

The grain sizes lie between a minimum and a maximum value,  $s_{\text{min}}$  and  $s_{\text{max}}$  where we fix the maximum grain size to 10 cm. Larger grains do not contribute to the SED in the wavelength range observed for the size distributions considered here with  $q_{\text{SED}} > 3$ . In addition, we fix the radial parameters to the values inferred from our resolved images (see Table 5). Therefore, we are left with three free parameters to fit: the minimum grain size,  $s_{\text{min}}$ , the size distribution index,  $q_{\text{SED}}$ , and the amount of dust,  $M_{\text{dust}}$ , for particles between  $s_{\text{min}}$  and  $s_{\text{max}}$  assuming a bulk density  $\rho$ .

We follow the three criteria given in Ballering et al. (2013) and Pawellek et al. (2014) to check for the presence of a warm component for the five discs. For us to consider a warm component to be present, there has to be a significant excess ( $\geq 3\sigma$ ) in either the WISE/22 or the MIPS/24 in excess of that which could originate in a single ring fitted to longer wavelength data. Secondly, the fit of the two-component SED has to be much better than the one-component fit. While the former studies assumed a better two-component fit when  $\chi^2_{\text{one}}/\chi^2_{\text{two}} > 3$  was fulfilled, we use the Bayesian information criterion instead, which is

$$\text{BIC} = \chi^2 + J \log_e(N), \quad (5)$$

where  $J$  represents the number of free parameters and  $N$  the number of data points. We use the classification given in Kass & Raftery (1995) to infer whether a one- or a two-component model is more likely. As a third criterion, we require the inferred ring containing the warm dust to be located outside the sublimation radius  $R_{\text{sub}}$  (assuming 1300 K as the sublimation temperature).

If all three criteria are fulfilled, we obtain the two-component model in the following way. In a first step, we assume the warm dust to be modelled by a pure blackbody to infer its blackbody temperature and radius. We assume this radius to be the location of the warm dust belt and fix the belt width to  $\Delta R_{\text{disc}}/R_{\text{disc}} = 10$  per cent. Finally, we fit both disc components assuming that the warm and cold dust ring possess the same size distribution of dust grains.

Similar to the cold dust ring, it is likely that the sub-mm disc radius of the warm belt is larger than the blackbody radius. Applying the newly inferred values presented in Section 4.4, the factor would be  $\sim 2.5$ , but it could be smaller or larger, since a consistently different dust temperature or composition could result in a systematic difference.

For the disc around HD 160305, only four mid- and far-infrared data points (WISE12, WISE22, PACS70, PACS160) are listed in the literature. Therefore, we fix the size distribution index,  $q_{\text{SED}}$ , to 3.5 (the outcome of an ideal collisional cascade, Dohnanyi 1969) to reduce the number of free parameters.

### 5.2 Fitting results

Following the criteria for two-component models, we checked at first the SEDs of the four resolved discs around HD 15115, HD 164249, HD 181327, and HD 191089 for the presence of a warm inner component. Only HD 15115 fulfills all of them so that we fitted this disc with a two-component model. The SED fitting results of the whole sample are all summarized in Table 3 and the SEDs are depicted in Fig. 1.

Collisional evolution models show that grains smaller than a certain blow-out size,  $s_{\text{blow}}$ , are expelled from the stellar system

due to radiation pressure. The blow-out size depends on the optical parameters of the dust material and increases with increasing stellar luminosity. We would expect the minimum grain size,  $s_{\min}$ , to be comparable to  $s_{\text{blow}}$ . However, previous studies of grain-size distributions (e.g. Pawellek et al. 2014; Pawellek & Krivov 2015) found that  $s_{\min}$  is weakly connected to the stellar luminosity. It might also be consistent with being independent of stellar luminosity, since those studies found an average value of  $\sim 5 \mu\text{m}$  to fit the majority of debris discs analysed therein. It was also found that the ratio between  $s_{\min}$  and  $s_{\text{blow}}$  is  $\sim 4 \dots 5$  for discs around host stars with stellar luminosities between 2 and  $5 L_{\text{sun}}$  (Pawellek et al. 2014). The  $s_{\min}/s_{\text{blow}}$  ratio is thought to be connected to the dynamical excitation of the planetesimals producing the visible dust (e.g. Krijt & Kama 2014; Thébault 2016). Earlier studies, such as Krivov, Löhne & Sremčević (2006), or Thébault & Augereau (2007), suggest a value around 2 for collisionally active discs.

For three targets in our sample, our modelling finds that  $s_{\min}$  is close to  $s_{\text{blow}}$  leading to a  $s_{\min}/s_{\text{blow}}$  ratio of  $\sim 1$ . Only the results for HD 15115 reveal an  $s_{\min}$  close to  $5 \mu\text{m}$  and an  $s_{\min}/s_{\text{blow}}$  ratio of  $\sim 5$ . However, the difference in  $s_{\min}$  of this disc to the others in the sample should be treated with caution, since the minimum grain size that we infer may be influenced by how we treated the warm component that is present only in this system. Besides our four targets, there is a range of different discs at the same stellar luminosity investigated by Pawellek & Krivov (2015) and Matrà et al. (2018) and shown as black dots in Fig. 3, most of which possess a larger  $s_{\min}$ . The low  $s_{\min}/s_{\text{blow}}$  ratio for F stars in the BPMG, which is reported for the first time, could indicate high levels of dynamical excitation similar to that found for discs around A-type stars (see fig. 16 in Pawellek & Krivov 2015).

The size distribution index,  $q_{\text{SED}}$ , lies between 3.4 and 3.8 for our sample. These values are consistent with collisional models (e.g. Löhne, Krivov & Rodmann 2008; Gáspár et al. 2012; Kral, Thébault & Charnoz 2013; Löhne et al. 2017).

Overall, the results from our SED modelling suggest that all four spatially resolved discs are in agreement with a stirred debris disc scenario, which means that the dust seen in the SED is consistent with being created by the collisional destruction of planetesimals in a belt traced by the ALMA images.

## 6 COMPARISON WITH NEARBY F STARS

In the first part of this study, we analysed the properties of the BPMG in detail. So far, we do not know whether the high-incidence rate of debris discs is a peculiarity of said moving group or whether we see more discs due to the young age of the moving group. Therefore, we will put the results of the BPMG into context with discs around other near-by F-type stars in the second part of this study. First, we investigate the evolution of spectral type to ensure that we compare stellar populations with similar properties. Then we look at the appropriate systems in samples of field stars and other young moving groups.

### 6.1 Stellar population at different ages

The stellar spectral type is determined by the effective temperature of the star. Due to ongoing thermonuclear reactions, stars and their physical/chemical properties, such as metallicity, stellar radius, or temperature, evolve over time so that the spectral type might change as well. Therefore, it is not self-evident that comparing stars with similar spectral types but different ages show the same stellar population at varying evolutionary phases.

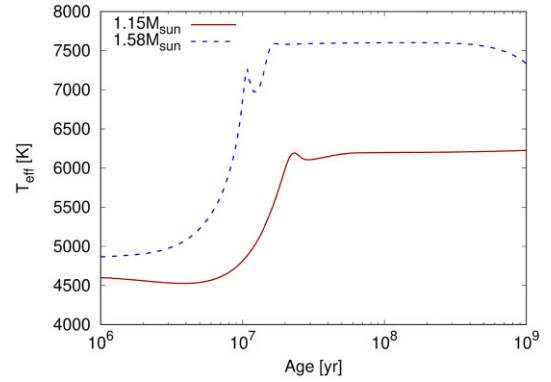


Figure 4. Stellar temperature as function of age.

We use the ‘Modules for Experiments in Stellar Astrophysics’ (MESA, Paxton et al. 2011, 2013, 2015; Choi et al. 2016) to check the evolution of stellar temperature over time. MESA consists of a one-dimensional stellar evolution module simultaneously solving the fully coupled structure and composition equations. The results are shown in Fig. 4. We use the lowest ( $1.15 M_{\text{sun}}$ ) and highest ( $1.58 M_{\text{sun}}$ ) stellar masses in our sample of F stars to analyse its parameter space and assume a stellar metallicity of  $[\text{Fe}/\text{H}] = 0.0$ .

The stellar temperature increases up to an age of  $\sim 10$  Myr and then stays constant until  $\sim 1$  Gyr. Our sample of F stars belongs to the BPMG with an age of 23 Myr. Fig. 4 shows that at this age, the temperature is already constant so that the spectral type is not changing. As a result, stars with similar spectral types and ages between that of the BPMG and 1 Gyr should represent the same population of stars. As the stars leave the main sequence from their position in the HR diagram, the stellar temperature starts to decrease. Higher mass stars (e.g. that were A stars on the main sequence) evolve to become F stars as they leave the main sequence. Therefore, a sample of F stars may be contaminated by post-main-sequence (higher mass) F stars. Their fraction should be small in a volume-limited population since the number of high-mass stars is lower. Furthermore, those stars do not spend long on the post-main sequence looking like an F star before they noticeably evolve so that they should be possible to identify from their stellar luminosity.

### 6.2 Field stars

Sibthorpe et al. (2018) analysed an unbiased sample of 275 FGK stars including 92 F-type stars observed with *Herschel*/PACS in the DEBRIS survey. None of the F-types belong to the BPMG, which lie within 24 pc. All targets are older than 160 Myr following the age determination of Vican (2012) with the exception of the targets HD 56986 with an age of  $\sim 20$  Myr and HD 7788A where no age is given.

Based on Sibthorpe et al. (2018), 22 of the 92 stars show evidence for a debris disc. However, we note that the target HD 19994 (Wiegert, Faramaz & Cruz-Saenz de Miera 2016) previously assumed to have spatially resolved IR emission shows evidence of being confused rather than possessing an actual disc (Yelverton et al. 2019). Thus, we update the number of detections for F stars in the DEBRIS sample to 21 out of 92 targets leading to a detection rate of  $22.8^{+6.2}_{-4.9}$  per cent. Due to the large beam size of *Herschel*/PACS, other targets might show confusion as well. However, after checking the PACS images available, we did not identify more potentially confused discs. The HR-diagram of the whole DEBRIS sample is presented in figs 1 and 2 in Phillips et al. (2010) and shows that all F stars in the DEBRIS

**Table 7.** F stars in the DEBRIS sample with debris disc detections.

HD	d (pc)	SpT	$L/L_{\text{sun}}$	$f_d$ ( $10^{-5}$ )	$R_{\text{BB}}$ (au)	$R_{\text{FIR}}$ (au)	$\Delta R_{\text{FIR}}$ (au)
1581	8.6	F9.5V	$1.29 \pm 0.01$	0.05	$124 \pm 45$	–	–
7570	15.2	F9VFe + 0.4	$1.96 \pm 0.01$	1.20	$28 \pm 10$	–	–
10647 <sup>a</sup>	17.3	F9V	$1.55 \pm 0.01$	32.7	$25 \pm 6$	$112.3 \pm 2.5$	$69.4 \pm 2.5$
11171	23.2	F0V	$5.80 \pm 0.10$	0.68	$32 \pm 17$	–	–
16673	21.9	F8VFe-0.4	$1.93 \pm 0.02$	0.33	$33 \pm 23$	–	–
22484 <sup>a</sup>	14.0	F9IV-V	$3.22 \pm 0.06$	0.72	$21 \pm 8$	$39.7 \pm 20.5$	$29.4 \pm 20.5$
27290 <sup>a</sup>	20.5	F1V	$6.67 \pm 0.09$	1.53	$77 \pm 23$	$151.2 \pm 32.2$	$121.1 \pm 32.2$
33262	11.6	F9VFe-0.5	$1.47 \pm 0.01$	1.29	$6.1 \pm 2.9$	–	–
48682 <sup>a</sup>	16.7	F9V	$1.86 \pm 0.02$	4.74	$69 \pm 16$	$134.4 \pm 7.6$	$73.7 \pm 7.6$
55892	21.4	F3VFe-1.0	$5.68 \pm 0.07$	1.21	$2.1 \pm 1.5$	–	–
56986 <sup>b</sup>	18.5	F2VkF0mF0	$11.8 \pm 0.20$	160	$0.1 \pm 0.1$	–	–
90089 <sup>a</sup>	22.7	F4VkF2mF2	$3.31 \pm 0.04$	1.01	$140 \pm 37$	$58.1 \pm 30.8$	$34.9 \pm 30.8$
102870	10.9	F9V	$3.73 \pm 0.04$	0.06	$48 \pm 68$	–	–
109085 <sup>a</sup>	18.3	F2V	$4.85 \pm 0.09$	2.76	$67 \pm 18$	$150.4 \pm 10.6$	$56.7 \pm 10.6$
110897 <sup>a</sup>	17.6	F9VFe-0.3	$1.11 \pm 0.01$	1.89	$52 \pm 15$	$97.14 \pm 48.3$	$65.7 \pm 48.3$
128167	15.7	F4VkF2mF1	$3.22 \pm 0.03$	1.38	$8.3 \pm 22$	–	–
160032	21.2	F4V	$4.55 \pm 0.06$	0.29	$64 \pm 35$	–	–
165908 <sup>a</sup>	15.6	F7VgF7mF5	$2.87 \pm 0.07$	0.80	$150 \pm 36$	$138.5 \pm 40.8$	$64.4 \pm 40.8$
199260	21.3	F6V	$1.97 \pm 0.01$	1.57	$26 \pm 12$	–	–
219482 <sup>a</sup>	20.5	F6V	$1.90 \pm 0.01$	3.26	$15 \pm 6$	$20.6 \pm 12.2$	$12.3 \pm 12.2$
222368	13.7	F7V	$3.33 \pm 0.03$	0.98	$5.9 \pm 6.7$	–	–

<sup>a</sup>Target was reported in Sibthorpe et al. (2018) to possess extended disc emission. The radii,  $R_{\text{FIR}}$ , from *Herschel*/PACS were derived from the model presented in Yelverton et al. (2019) and are defined in the same way as described in Section 4.3.2. <sup>b</sup>HD 56986 possesses a marginal excess at MIPS24. The image at PACS160 seems to be confused with a nearby background object making the SED model very uncertain.

sample, which possess debris discs, are compatible with belonging to the main sequence. Therefore, we assume that in the DEBRIS sample, no debris discs around post-main-sequence F stars are included.

The SEDs are fitted using the same process outlined in Section 4.3.2. The modelling results are listed in Table 7 and the SEDs are shown in Figs A3 and A4. We find blackbody radii between 2 and 200 au for the whole sample with the exception of HD 56986 with a blackbody radius around 0.1 au based on a marginal mid-IR excess. The excess found at PACS160 is confused by a nearby background object so that the SED model is very uncertain. We therefore exclude this target from our further analysis.

Ignoring HD 56986 due to the aforementioned reasons, we find no discs smaller than 1 au, one disc out of 92 targets with a blackbody radius between 1 and 3 au (1.1 per cent), three disc radii between 3 and 10 au (3.3 per cent), five discs between 10 and 30 au (5.4 per cent), seven discs between 30 and 100 au (7.6 per cent), and four discs larger than 100 au (4.3 per cent). Nine targets were reported to be spatially resolved in the FIR (Sibthorpe et al. 2018) (excluding HD 19994). Only HD 10647 and HD 109085 were observed with ALMA (see Section B3). However, using the method of Yelverton et al. (2019), we infer radii and disc widths from *Herschel*/PACS images in the same manner as described in Section 4.3.2 (see Table 7). The discs range from 20 au to more than 150 au. The smallest discs are located around HD 22484 and HD 219482 with radii of 39.7 and 20.6 au, respectively. The disc widths are uncertain because of the relatively poor spatial resolution so that we cannot draw strong conclusions on them.

### 6.3 Other young moving groups

The question arises whether the high occurrence rate of debris discs around F-type stars in BPMG is a singular phenomenon of this moving group or if it is common in other associations with comparable properties in age and distance as BPMG. Here, we

compare the BPMG disc incidence rates with those of other clusters. When doing so, we need to recognize that some stars lack FIR data and so have limited constraints on the presence of circumstellar dust. We will consider detection rates for the whole sample (e.g. the 9/12 rate from the BPMG) and separately we will consider the rate among those with FIR data (e.g. the 9/11 rate for the BPMG).

Following studies of young associations (e.g. fig. 7 in Gagné, Faherty & Mamajek 2018c; Gagné & Faherty 2018) we identified five groups with similar peaks in their distance distributions around 50 pc comparable to the BPMG: the Tucana/Horologium association (THA), Columba (COL), Carina (CAR), AB Doradus (ABDMG), and Carina-Near (CARN). The groups THA, COL, and CAR possess an age around  $\sim 45$  Myr, the groups ABDMG and CARN possess an age around  $\sim 150$  Myr. For the purpose of our analysis, a differentiation between the single moving groups is not necessary. Indeed, Torres et al. (2008) and Zuckerman et al. (2011) found that THA, COL, and CAR are closely located, making it difficult to place members in one or the other group. Therefore, we generated two samples, one referred to as 45-Myr group that sums up all F-type targets belonging to THA, COL, and CAR, the other referred to as 150-Myr group that combines the targets of ABDMG and CARN. Both samples are unbiased towards the presence of IR-excess.

Using the studies of members of young moving groups (Zuckerman et al. 2011; Faherty et al. 2018; Gagné et al. 2018b; Gagné & Faherty 2018), we identified 29 F stars in Table 8 for the 45-Myr group and 13 for the 150-Myr group. For several targets, only data up to mid-infrared wavelengths (WISE22) are available or upper limits from IRAS at 25, 60, and 100  $\mu\text{m}$  but no *Spitzer*/MIPS or other FIR data. The presence of FIR emission for these targets cannot be ruled out, but none of their SEDs shows excess in the mid-infrared. The detection rates are listed in Table 9 and given for both the complete samples and the sub-samples only including targets with FIR data.



**Table 8.** F stars of the 45 and 150 Myr groups.

HD	Group	d (pc)	SpT	$L/L_{\text{sun}}$	Disc excess	$f_d$ ( $10^{-5}$ )	$R_{\text{BB}}$ (au)
984	45 Myr	45.9	F7V	$2.04 \pm 0.02$	No	—	—
1466	45 Myr	43.0	F8V	$1.58 \pm 0.01$	Yes	6.3	$7.8 \pm 1.8$
8671	45 Myr	42.7	F7V	$6.08 \pm 0.04$	...	...	...
10269	45 Myr	46.7	F5V	$2.60 \pm 0.02$	Yes	12	$8.8 \pm 5.2$
10863	45 Myr	45.0	F2V	$4.39 \pm 0.03$	No	—	—
12894	45 Myr	46.3	F4V	$4.50 \pm 0.04$	No	—	—
13246	45 Myr	45.6	F7V	$1.72 \pm 0.04$	Yes	14	$5.4 \pm 1.4$
14691	45 Myr	30.0	F3V	$4.76 \pm 0.04$	No	—	—
17250	45 Myr	57.1	F8	$1.91 \pm 0.02$	...	...	...
20121	45 Myr	42.5	F3V+A8V	$5.70 \pm 0.60$	...	...	...
20385	45 Myr	48.8	F6V	$2.08 \pm 0.02$	No	—	—
21024	45 Myr	29.3	F5IV-V	$4.25 \pm 0.03$	...	...	...
24636	45 Myr	57.1	F3IV/V	$3.66 \pm 0.02$	Yes	9.9	$13 \pm 3$
29329	45 Myr	32.7	F7V	$2.25 \pm 0.02$	...	...	...
30051	45 Myr	67.6	F2/3IV/V	$5.20 \pm 0.20$	Yes	3.0	$48 \pm 19$
30132	45 Myr	121	F6/7V	$3.03 \pm 0.03$	...	...	...
30447	45 Myr	80.5	F3V	$3.68 \pm 0.03$	Yes	92	$34 \pm 8$
30984	45 Myr	82.6	F5V	$2.09 \pm 0.02$	...	...	...
31359	45 Myr	112	F5V	$3.30 \pm 0.20$	...	...	...
32195	45 Myr	62.8	F7V	$1.34 \pm 0.01$	Yes	8.5	$14 \pm 7$
35114	45 Myr	47.7	F6V	$2.08 \pm 0.02$	Yes	4.0	$6.4 \pm 2.7$
35996	45 Myr	92.1	F3/5IV/V	$3.40 \pm 0.03$	Yes	9.1	$3.9 \pm 2.1$
37402	45 Myr	69.6	F6V	$0.82 \pm 0.03$	No	—	—
37484	45 Myr	59.1	F4V	$3.49 \pm 0.02$	Yes	31	$18 \pm 5$
40216	45 Myr	52.8	F7V	$2.38 \pm 0.02$	No	—	—
43199	45 Myr	76.8	F0III/IV	$4.88 \pm 0.05$	...	...	...
53842	45 Myr	57.9	F5V	$2.84 \pm 0.02$	Yes	1.9	$93 \pm 16$
207575	45 Myr	47.0	F6V	$2.31 \pm 0.02$	No	—	—
207964	45 Myr	46.5	F0V+F5V	$9.90 \pm 0.4$	No	—	—
3454	150 Myr	45.4	F5	$1.69 \pm 0.02$	...	...	...
4277	150 Myr	52.5	F8V	$1.70 \pm 0.10$	No	—	—
15407	150 Myr	49.4	F5V	$3.23 \pm 0.03$	Yes	430	$1.01 \pm 0.35$
25457	150 Myr	18.8	F7V	$2.05 \pm 0.01$	Yes	13.0	$17 \pm 4$
25953	150 Myr	57.0	F6V	$1.97 \pm 0.02$	No	—	—
31949	150 Myr	63.1	F8V	$1.84 \pm 0.02$	...	...	...
61518	150 Myr	61.5	F5V	$2.18 \pm 0.02$	No	—	—
69051	150 Myr	84.7	F0III	$9.27 \pm 0.09$	...	...	...
103774	150 Myr	56.5	F6V	$3.62 \pm 0.03$	...	...	...
121560	150 Myr	24.5	F6V	$1.70 \pm 0.01$	No	—	—
218382	150 Myr	192	F8	$8.10 \pm 0.20$	...	...	...
219693	150 Myr	34.1	F4V	$5.66 \pm 0.06$	...	...	...
CD-26 1643	150 Myr	54.8	F9V	$1.24 \pm 0.01$	No	—	—

*Note.* The data are taken from Zuckerman et al. (2011), Faherty et al. (2018), Gagné et al. (2018b), and Gagné & Faherty (2018). The excess emission is given for *Spitzer*/MIPS at 24  $\mu\text{m}$  and/or 70  $\mu\text{m}$ . The excess emission for stars with only WISE22 data or upper limits from IRAS is shown as dots. The fractional luminosities are inferred from a modified blackbody SED model.

**Table 9.** Detection rates for the different samples.

Sample	$N_{\text{Discs}}$	$N_{\text{total}}$	$N_{\text{FIR}}$	Rate <sub>total</sub> (%)	Rate <sub>FIR</sub> (%)
BPMG	9	12	11	$75.0^{+25.0}_{-24.5}$	$81.8^{+18.2}_{-26.8}$
45 Myr	11	29	20	$37.9^{+15.2}_{-11.3}$	$55.0^{+22.1}_{-16.3}$
150 Myr	2	13	7	$15.4^{+20.3}_{-9.9}$	$28.6^{+37.7}_{-28.5}$
DEBRIS	21	92	92	$22.8^{+6.2}_{-4.9}\%$	$22.8^{+6.2}_{-4.9}\%$

*Note.*  $N_{\text{Discs}}$  gives the number of disc detections,  $N_{\text{total}}$  is the total number of targets in the sample,  $N_{\text{FIR}}$  is the number of targets with FIR data. The detection rates are given for the complete samples and the sub-samples composed of targets with FIR data assuming the number of disc detections,  $N_{\text{Discs}}$  divided by the sample size. The uncertainties were calculated using the method of Gehrels (1986).

We applied the same modified blackbody model to fit the SEDs of systems in the 45 Myr and 150 Myr groups (see Figs A1 and A2) and inferred stellar parameters, fractional luminosities, and blackbody radii using the same method as in Section 3 (see Table 8). In the 45-Myr group, we find no disc with a blackbody radius below 1 au. Two out of 29 targets possess belts with blackbody radii between 1 and

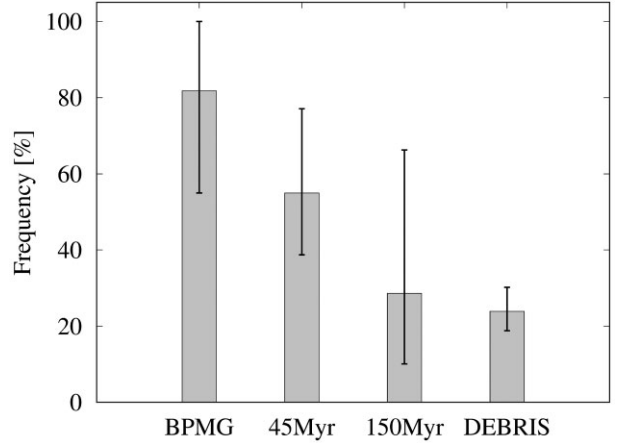


**Figure 5.** Incidence rates for the different samples ordered by age: BPMG (23 Myr), 45-Myr group, 150-Myr group, and DEBRIS (>160 Myr). The uncertainties are calculated using the method of Gehrels (1986). Only targets with FIR data are taken into account (see Table 9). Frequencies are not corrected for completeness.

3 au (6.9 per cent), five discs lie between 3 and 10 au (17.2 per cent), two between 10 and 30 au, and two between 30 and 100 au (each 6.9 per cent). There were only two discs detected within the 150-Myr group. One lies at 1 au and the other at 17 au. We note that the disc around 1 au (HD 15407) is only poorly fitted since a strong solid state feature is visible in the SED but that the conclusion of a small blackbody radius is reliable.

Considering NIR, FIR, or sub-mm disc radii, only HD 30447 was reported as spatially resolved in scattered light (Soummer et al. 2014) with a detection between 60 and 200 au.

#### 6.4 Comparing the samples

In Fig. 5, we compare the fractions of stars with debris disc detections for each sample, which suggests that there might be a decrease of disc frequency with increasing age. Using the DEBRIS sample as reference and Fisher's exact test (Fisher 1956), we tested the hypothesis that the incidence rates for the BPMG, the 45-Myr group, and the 150-Myr group are similar to the DEBRIS sample. We found that for the BPMG, the probability  $p = 7.9 \times 10^{-4}$ , for the 45-Myr group,  $p = 0.013$ , and for the 150-Myr group,  $p = 0.68$ . The hypothesis is rejected if the  $p$  value is smaller than a chosen significance level,  $\alpha$  which we set to 0.05. Therefore, we can say that for BPMG and the 45-Myr group, the detection rates are not similar to that of the DEBRIS sample. In addition, we tested whether the rates of the BPMG and the 45-Myr group are different from each other and found  $p = 0.45$ . This means that the BPMG and the 45-Myr group show similar detection rates. The result leads to the impression that a high frequency of debris discs might be common for F stars younger than 100 Myr.

#### 6.5 Fractional luminosity versus radius

Plotting detection rate versus age can be misleading, since different surveys reach different sensitivities to discs, for example due to the different distance of the stars in their samples. This sensitivity can be understood within the context of a modified blackbody model, since for each star the region of fractional luminosity versus blackbody radius for which a disc detection would have been possible can be readily quantified. Combining this information for all stars in a

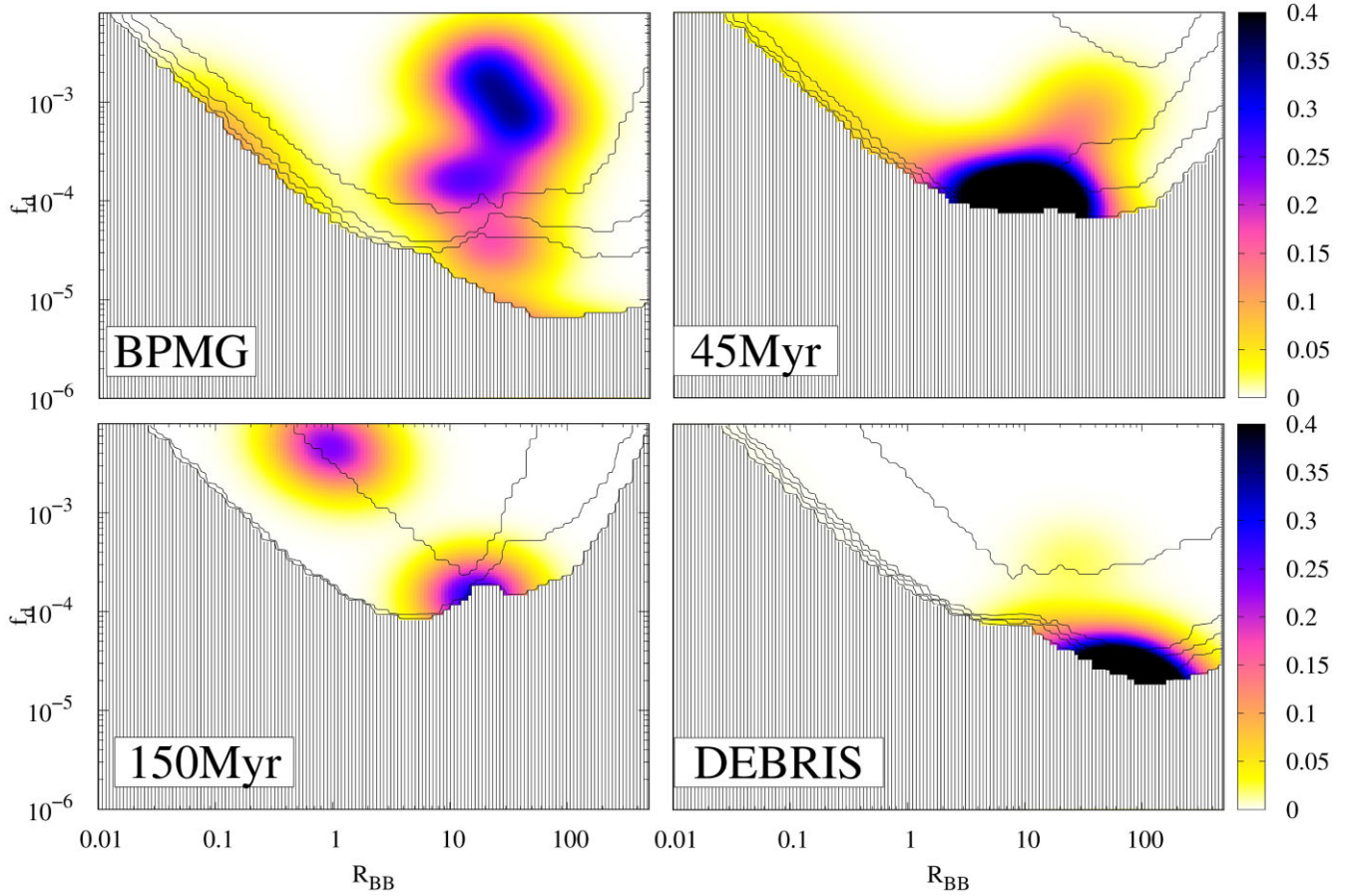


**Figure 6.** Fractional luminosity as function of blackbody radius for the four samples (BPMG, 45-Myr group, 150-Myr group, and DEBRIS). The colour scale shows the disc incidence, per log(au), per log(unit  $f_d$ ). The contour lines show the levels of completeness for 0.1, 0.3, 0.5, 0.7, and 1.0 starting from the bottom of the plot.

given sample, it is then possible to determine the fraction of stars for which discs could have been detected in different regions of parameter space. This is the basis of the approach taken in Fig. 6, which follows on from that used in Sibthorpe et al. (2018) and Wyatt (2018). There we plot the parameter space of fractional luminosity versus blackbody radius for the four samples of F stars (BPMG, the 45-Myr group, the 150-Myr group, and DEBRIS), noting that the sub-mm disc radius is expected to be  $\sim 2.5$  times larger than the blackbody radius (Section 4.4).

To estimate how many discs can be detected in a certain area of parameter space, we analysed the targets of each sample independently of whether they were reported to possess a disc or not. Using blackbody radii between 0.01 and 1000 au and fractional luminosities between  $10^{-7}$  and  $10^{-2}$ , we generated a grid of fiducial discs assuming a pure blackbody model. We inferred the flux density of each model disc at wavelengths corresponding to those of observations of each star, e.g. with WISE, *Spitzer*/MIPS, *Herschel*/PACS, and ALMA. If the total flux density of the fiducial model (star + disc) satisfied

$$F_\nu > F_\nu^{\text{star}} + 3\sqrt{(\Delta F_\nu^{\text{obs}})^2 + (\Delta F_\nu^{\text{star}})^2}, \quad (6)$$

with  $F_\nu^{\text{star}}$  being the flux density of the stellar photosphere,  $\Delta F_\nu^{\text{star}}$  its uncertainty, and  $\Delta F_\nu^{\text{obs}}$  being the uncertainty of the observation, we assumed the model disc to be detected at the wavelength analysed. A model disc is counted as a detection as soon as one wavelength

band fulfills equation (6). As a result, we get the area of parameter space where discs around a certain host star can be detected. For a given sample, we calculate the number of stars for which discs could be detected for each node of the grid generating the contour lines shown in Fig. 6. The contour lines are an estimate for the level of completeness of the disc detections. For example, if 10 discs are found at a location where discs could have been detected towards 50 per cent of stars, this suggests that the true number of discs at this location is  $10 \times 100/50$ , since for half of the stars the observations provide no information about the presence of discs at this level.

For the BPMG sample, we find that discs with blackbody radii of  $\sim 20$  au could be detected around 100 per cent of the stars at fractional luminosities of  $1 \times 10^{-4}$ . Discs around  $\sim 100$  au could be detected around 10 per cent of the stars for  $f_d = 6 \times 10^{-6}$ . For the 45-Myr group, discs at 100 au could be detected around 10 per cent of the stars for  $f_d = 7 \times 10^{-5}$  while for the 150-Myr group,  $f_d = 2 \times 10^{-4}$  and for the DEBRIS,  $f_d = 3 \times 10^{-5}$ . The reason for the different sensitivity limits is given by the observations themselves. Some targets have not been studied in detail so that we do not have data longwards of  $70 \mu\text{m}$  and only upper limits are available (e.g. from IRAS), which barely constrain the sensitivity limits.

A second aspect of Fig. 6 is the actual disc detections. They appear on the plot over the range of  $f_d$  and  $R_{\text{BB}}$  where they could appear according to their likelihood. The likelihood itself was inferred through SED fitting as described in Section 3. In Fig. 6, we use the colour scale to show the fraction of stars for which discs are

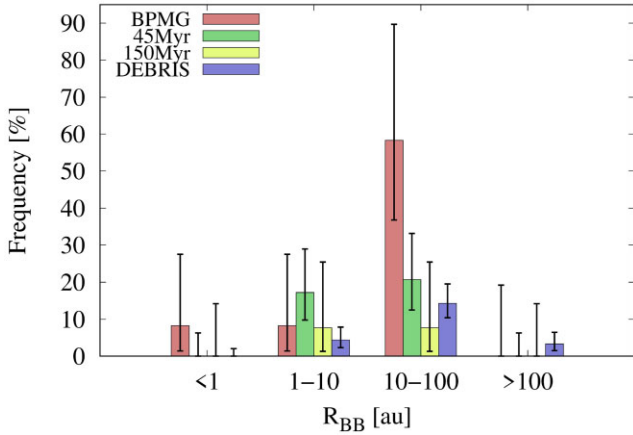


**Figure 7.** Frequency of disc radii for different radius bins assuming the total number of targets in each sample taken from Table 9. The uncertainties were calculated using Gehrels (1986).

present. The scale gives the incidence rate of a disc per log (au), per log ( $\text{unit} f_d$ ), per number of targets in the sample. The incidence rate has been corrected for completeness by dividing the observed incidence rates by the sensitivity limits given by the contour lines and was then smoothed with a Gaussian by one order of magnitude in blackbody radius and fractional luminosity.

Although discs could have been detected down to fractional luminosities of  $\sim 10^{-6}$ , we find that the majority of discs in the BPMG sample is located around  $f_d = 10^{-3}$ , the area where 100 per cent of fiducial discs can be detected. The 45-Myr group and DEBRIS discs are found in areas closer to the sensitivity limits ( $f_d = 7 \times 10^{-5}$  for the 45-Myr group,  $f_d = 3 \times 10^{-5}$  for DEBRIS), some in areas where less than 10 per cent of the model discs are observable, which results in a higher corrected incidence rate. For the 150-Myr group, we have only two disc detections, one lying within the area of 100 per cent completeness the other close to the detection limit.

Assuming that Fig. 6 shows comparable debris disc populations at different ages starting from 23 Myr (BPMG) over 45 Myr to older field stars (DEBRIS), we see a decay of fractional luminosity with increasing age, which is in agreement with Fig. 5 where we see a decrease in detection rates. While we would expect such a decrease due to collisional evolution, it seems that the process takes place in the first 100 Myr (see Section 7.1). Furthermore, the blackbody radii seem to show a slight increase from the BPMG ( $\sim 30$  au) to the DEBRIS ( $\sim 100$  au). Possible reasons, besides observational biases, will be discussed in Section 6.6.

## 6.6 Radius distribution

In this section, we compare the radii of discs found in the BPMG with those of other young moving groups and field stars. Since most of the targets are not spatially resolved, we will look at both blackbody and spatially resolved disc radii to identify possible differences between the samples.

### 6.6.1 Blackbody radii

We focus on the SED results listed in Tables 3, 7, and 8 that were used to produce Fig. 6. We compare the blackbody radius of each sample in Fig. 7 applying four radius bins in logarithmic spacing:  $R_{\text{BB}} < 1$  au comparable to hot dust,  $1 - 10$  au comparable to the warm asteroid belt,  $10 - 100$  au comparable to the cold Kuiper belt,

and  $\geq 100$  au for larger discs. The frequencies plotted are taken from Table 9 by comparing the number detected with the total number of targets in each sample, noting that there could be more discs in each radius bin that are below the detection threshold. Most of the discs are found with blackbody radii between 1 and 100 au. For the BPMG sample and the 45 Myr group, the majority lies between 10 and 30 au and for the DEBRIS sample between 30 and 100 au.

The latter is the only sample containing discs with blackbody radii larger than 100 au. The DEBRIS sample has a detection limit for large discs down to  $f_d = 3 \times 10^{-5}$  (Fig. 6) where the 45-Myr group shows discs only when  $f_d > 7 \times 10^{-5}$ , while in the 150-Myr group discs must be brighter than  $f_d = 2 \times 10^{-4}$  to be detected. Thus, it is possible that we miss those large and faint discs in the 45-Myr and 150-Myr groups as they would lie below the respective detection limits. In the BPMG, however, the detection limit lies at  $6 \times 10^{-6}$  and is lower than for the DEBRIS sample. Yet, we did not find any large discs in the BPMG. This might be a result of the low number of targets compared to the DEBRIS sample. For example, the probability of detecting one or more  $> 100$  au disc in the BPMG sample of only 12 stars would be 41.3 per cent if their incidence rate was the same as that of the DEBRIS sample of 4/92.

Nevertheless, it seems that the discs in moving groups (BPMG, 45-Myr group) tend to be smaller compared to discs around field stars as seen in DEBRIS (see Section 6.5). It could be a systematic increase in physical size with increasing age, or that discs in young moving groups are hotter (and so appear smaller by the  $R_{\text{BB}}$  metric) than around older stars. Smaller discs in young moving groups might be expected from collisional theory as those could have been depleted around older field stars (see Section 4.2.4 of Wyatt et al. 2007). On the other hand, the discs in the BPMG possess a high fraction of small grains (see Section 5) while the particles around comparable field stars are found to be larger (Pawellek & Krivov 2015). This might support the idea of hotter discs in young moving groups. Nevertheless, the number of targets in each sample is small and the uncertainties are large so that we cannot draw strong conclusions on the difference in the radius distribution. We will consider the influence of collisional evolution in more detail in Section 7.

### 6.6.2 Spatially resolved disc radii

In this section, we compare the NIR, FIR, and sub-mm radii inferred from spatially resolved observations from ALMA, *Herschel*/PACS, and VLT/SPHERE data. Using ALMA, four targets were resolved in the BPMG and two discs (HD 10647 and HD 109085, Table B1) in the DEBRIS sample. With *Herschel*/PACS, three discs in the BPMG and nine discs in the DEBRIS sample were resolved (Tables 5 and 7). Considering scattered light observations, four discs in the BPMG were resolved. In the 45 Myr group, only HD 30447 was reported as spatially resolved with SPHERE.

In Fig. 8, we compare the ALMA radii to the *Herschel*/PACS and VLT/SPHERE radii for the BPMG and DEBRIS to infer possible biases between the values from the different observations. In Section 4.3.2, we already found that the *Herschel* and ALMA radii for the BPMG are in good agreement. This is also the case for HD 109085 from the DEBRIS sample, while for HD 10647, the *Herschel* radius seems larger compared to ALMA. Additionally, SPHERE data show broad extended discs for HD 15115, HD 181327, and HD 191089 with the location of the surface brightness peak being in good agreement with the ALMA radii as well.

Fig. 8 complements the results found in Pawellek et al. (2019). That study used collisional models and showed that at high resolution, the

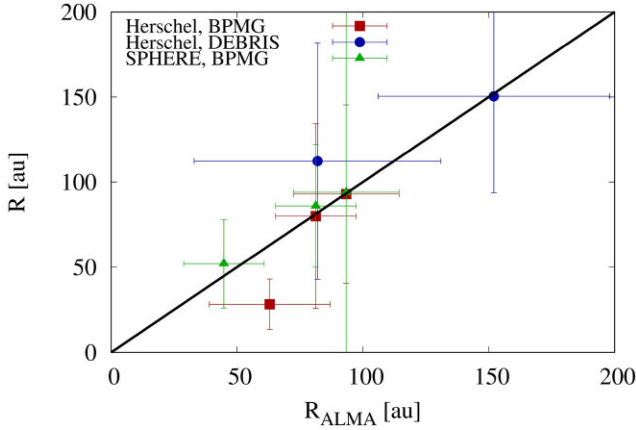


**Figure 8.** Resolved disc radii inferred from *Herschel*/PACS and VLT/SPHERE compared to ALMA radii. The central radius of *Herschel* is assumed to be  $0.5 \times (R_{\text{in, FIR}} + R_{\text{out, FIR}})$ . The error bars indicate the disc width inferred from observations.

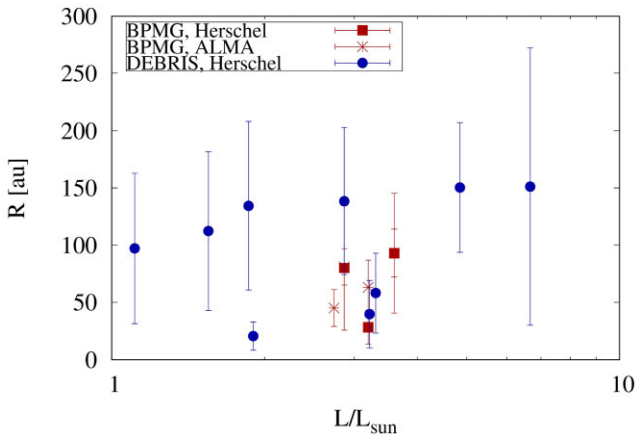


**Figure 9.** Resolved disc radii of the BPMG and DEBRIS as function of stellar luminosity. The radii are inferred from *Herschel* and ALMA images. The error bars indicate the disc width.

peak of the discs' surface brightness is at the same location in sub-mm and FIR images (and is nearly coincident with the planetesimal belt). However, the low surface brightness halo made of small grains that extends beyond the belt gets brighter at shorter wavelengths. It is thus possible that due to the halo and the lower resolution of *Herschel*, the radii inferred from *Herschel* could appear larger than ALMA radii, which might be the case for HD 10647. Based on Fig. 8, we assume that the disc radii inferred from different telescopes give comparable values.

In Fig. 9, the FIR and sub-mm radii of the BPMG and DEBRIS sample are shown as a function of stellar luminosity with error bars indicating the disc width. There are three discs in the DEBRIS sample with FIR radii below 50 au, but the majority of targets (six) possesses radii around  $\sim 100$ – $150$  au. All discs are found to be broad. Five of the discs with FIR radii between 100 and 150 au also possess blackbody radii larger than 50 au (Table 7) and are in agreement with an expected ratio of sub-mm to blackbody radius ratio of  $\sim 2.5$  (Section 4.4). In contrast to the DEBRIS sample, the discs in the BPMG are found within 100 au.

Nevertheless, we have to keep in mind that while most of the discs in the DEBRIS sample are larger than the discs in the BPMG, the number of spatially resolved discs in both samples is low.

Furthermore, seven of the nine resolved discs in DEBRIS were observed with *Herschel*/PACS but not with ALMA. *Herschel*/PACS has a lower spatial resolution and thus might bias the sample of resolved discs towards larger radii.

## 7 ORIGIN OF HIGH DETECTION RATE

We found that the detection rate for debris discs around F-type stars is significantly higher in the BPMG than in the DEBRIS sample. In this section, we investigate different scenarios that might explain this phenomenon:

(i) The BPMG is representative of the population of stars that become field stars. Hence, the discs seen in both the BPMG and DEBRIS samples are essentially the same population but seen at different ages. This is considered in Section 7.1.

(ii) The BPMG is representative of the population of stars that become field stars. However, the discs seen in BPMG and DEBRIS are not the same population seen at different ages. This is considered in Section 7.2.

(iii) The BPMG is not representative of the population of stars that become field stars, since the environment of young moving groups is different to that in which field stars formed and more conducive to the retention of bright discs. This is considered in Section 7.3

### 7.1 Same population scenario

In the first scenario, we assume that the BPMG and DEBRIS samples possess the same population of discs seen at different ages. Therefore, the discs in the BPMG should evolve into discs comparable to the DEBRIS sample. To describe the evolution process, we use the collisional evolution model (Section B) and assume that the disc radius stays constant while the fractional luminosity decreases over time.

If the largest planetesimals are in collisional equilibrium at the age of the BPMG, then the fractional luminosity decreases with  $f_d \propto 1/t$ , where  $t$  is the time (see equation B2). However, it could also have decreased less than this or even stayed constant if the biggest bodies were not yet in collisional equilibrium.

#### 7.1.1 Modelling detection rates

To predict the population that the BPMG would evolve into by DEBRIS ages, we make a generic model. We generate 100 000 artificial samples of 92 targets similar to the size of the DEBRIS sample. Each target is randomly chosen from the 12 systems of the BPMG sample so that each artificial sample is completely made of BPMG targets including those without a disc detection. We assume that the fractional luminosity follows

$$f_d(t) = f_d(t_0) \left( \frac{t}{t_0} \right)^{-\alpha}, \quad (7)$$

with  $f_d(t_0)$  being the fractional luminosity at the time  $t_0$  and  $\alpha$  being a free parameter. DEBRIS is an unbiased sample of field stars and as such its stars should possess random ages up to the main-sequence lifetime. We therefore generate random ages ( $t$ ) for the 92 targets in each of our artificial samples and calculate the fractional luminosity  $f_d(t)$  using those inferred from SED modelling of the BPMG sample as values for  $f_d(t_0)$ . In the next step, we consider the parameter space ( $R_{\text{BB}}, f_d(t)$ ) as shown in Fig. 6. For each location, we know the probability that a star in the sample was observed with sufficient sensitivity to detect the disc. We generate a random number between



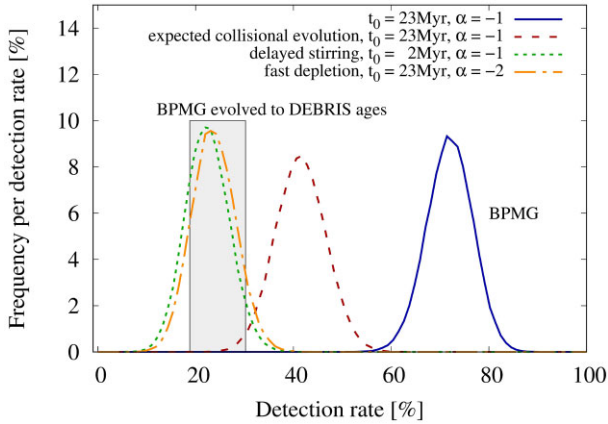


**Figure 10.** Detection rates of a sample made of 92 discs around F-type stars similar to DEBRIS with disc properties similar to the discs in BPMG. The grey region shows the detection rate inferred from the DEBRIS sample ( $23.9^{+6.3}_{-5.1}$  per cent Sibthorpe et al. 2018).

0 and 1 for each target in the 100 000 samples and compare it to the probability of detecting the disc at its location of parameter space. If the probability is larger than this random number, we count the disc as a detection. For each of the 100 000 generated samples, we assume that the probability to detect a disc at a certain location ( $R_{BB}$ ,  $f_d(t)$ ) is comparable to that of the actually observed DEBRIS sample as shown in Fig. 6. As a result, we get a distribution of detection rates for the 100 000 artificial samples, which is shown in Fig. 10.

To test the model, we considered what it would predict for the BPMG, i.e. for a set of 100 000 samples each containing 12 targets randomly taken from the actual BPMG sample with the same age as the BPMG. We applied the disc detection probability distribution inferred for BPMG. In Fig. 10, the solid blue line shows the resulting distribution of detection rates peaking around 75 per cent similar to the actual BPMG sample.

### 7.1.2 Expected detection rates

Given the derived age of the BPMG, we set  $t_0$  to 23 Myr and  $\alpha = -1$  as expected from the collisional evolution model (Wyatt et al. 2007). The dashed red line in Fig. 10 shows that in this case the DEBRIS sample should have a detection rate of  $41 \pm 10$  per cent following Poisson statistics with a 95 per cent confidence level. This is incompatible with the observed detection rate of  $22.8^{+6.2}_{-4.9}$  per cent for the DEBRIS sample. Since  $\alpha = -1$  is the fastest possible collisional evolution, this suggests that collisional evolution cannot be the explanation if the BPMG and DEBRIS samples possess the same population of discs at different ages.

### 7.1.3 Delayed stirring

The observed detection rate of the DEBRIS sample could be explained if the cascade was initiated only recently, i.e. if the collision age was closer to  $t_0 \sim 2$  Myr instead of the stellar age of 23 Myr, which is shown with the dotted green line in Fig. 10.

However, this is not realistic since protoplanetary discs dissipate within a few Myr (e.g. Pascucci et al. 2006). While delayed stirring is expected in some models (e.g. Kenyon & Bromley 2008), this explanation would require all discs to wait 21 Myr before being ignited, whereas all discs are located at different radii and so should have different evolution time-scales.

### 7.1.4 Fast depletion

The other explanation that is compatible with the assumption of similar disc populations in the BPMG and DEBRIS samples is that the evolution is faster than  $t^{-1}$ . The dash-dotted orange line in Fig. 10 shows that  $t^{-2}$  is in agreement with this hypothesis. However, such rapid evolution is no longer consistent with simple collisional evolution models. Collisional models might still be able to reproduce rapid evolution of disc luminosity if in addition to depletion of the large bodies there is also a change in the equilibrium dust-size distribution, e.g. an overabundance of small grains above steady state at BPMG ages.

There might be physical motivation for the dust-size distribution to evolve, say if the quantity of sub-blow-out grains destroying the larger particles is changing or if there is gas preventing small dust being removed at young ages. Indeed, the collision model introduced by Löhne et al. (2017) shows an increase in particles slightly larger than the blow-out size (e.g. fig. 6 in Löhne et al. 2017). However, there is no evidence for a change in small dust properties in the SED models'  $s_{\min}$  or  $q$ , and there is no significant gas in these systems. The only target with a gas detection is HD 181327 (see Section 4.2.3) for which Marino et al. (2016) found only low-gas masses making the presence of gas unlikely to influence the dust in this disc. Hence, gas is also unlikely to explain the fast depletion of the whole sample. This leads to the conclusion that something other than collisions is depleting the BPMG discs.

One potential problem with this scenario is that the evolution with  $t^{-2}$  suggested by our model is not compatible with other studies, which have shown that the discs of Sun-like stars evolve slowly on the main sequence. While ages are hard to determine for those stars, there seems to be slow evolution ( $\sim t^{-0.5}$ ) beyond a few 100 Myr (e.g. Trilling et al. 2008; Holland et al. 2017). However, the  $t^{-2}$  trend represents only an average evolution. A solution to this problem is thus that there is a process that depletes the BPMG discs that acts even faster than  $t^{-2}$  but only on time-scales of order 100 Myr following which the slower collisional depletion resumes for any remaining planetesimals that go on to supply the dust seen in the DEBRIS population.

The Solar System's Edgeworth–Kuiper belt underwent depletion by two orders of magnitude in mass on a time-scale of 10–100 Myr as a result of the dynamical instability in the planetary system, so this is one possibility (Gomes et al. 2005). Others could be embedded planetary embryos, or planets that migrate into the discs (e.g. Gomes et al. 2005; Levison et al. 2008; Izidoro, Morbidelli & Raymond 2014; Nesvorný 2015). Given the depletion time-scale inferred above, we use equation (3) of Shannon et al. (2016) to estimate the mass of potential planetary perturbers by setting the time-scale of such perturbers to clear their surrounding area from dust to 100 Myr. We find masses between 20 and 170 earth masses (corresponding to 1 and 10 Neptune masses). With currently available telescopes such planets could very well be undetected within the discs in the BPMG. Based on results from different observational instruments like *Kepler* or HARPS summarized in the exoplanet data base<sup>3</sup> (Schneider 2011),  $\sim 260$  close-in planets were detected around F-type stars by radial velocity or transit observations,  $\sim 50$  of them possessing masses between 1 and 10 Neptune masses. This is just an estimate, since in many cases the total masses of the planets could not be inferred. Furthermore, most of the planets detected are located close to the host star and are far away from the typical debris

<sup>3</sup><http://exoplanet.eu/>

discs investigated in our study. Suzuki et al. (2016) analysed data from the Microlensing Observations in Astrophysics and estimate that cold Neptunes located beyond the snow line of stellar systems and thus closer to debris discs might be more common than their close-in hot siblings.

51 Eri is the only system with a planet detection in our sample. Due to a lack of spatially resolved images of the disc, we cannot rule out that the Jupiter-mass planet might be located close to the disc and thus accelerating its depletion. An indicator for this scenario could be the already low disc's fractional luminosity of  $5 \times 10^{-6}$ . Indeed, a Jupiter-mass planet located within our BPMG discs would only need  $\sim 20$  Myr to clear its surrounding area (equation 3, Shannon et al. 2016).

Another possible depletion mechanism is the disintegration of planetesimals due to heating. Lisse et al. (2020) showed that high-energy stellar flares are able to heat dust in close-in debris discs to temperatures of  $\sim 1000$  K. According to studies of Kepler/K2 stars (Davenport 2016; Van Doorsselaere, Shariati & Debosscher 2017), 1.6 per cent of young F-type stars show such flares. However, the majority of the discs in the BPMG lie too far out ( $\sim 80$  au) for this to be important. The close-in disc around HD 199143 might be a candidate for such a depletion mechanism though collisions would be expected to deplete this disc by DEBRIS ages (Wyatt et al. 2007).

Planetesimals could also be depleted by stellar radiation forces such as the YORP effect. However, the relatively slow evolution of Solar system asteroids (Đurech et al. 2018) suggests that this radiation effect might be negligible, since it should be weaker for planetesimals at several tens of au.

## 7.2 Two population scenario

In Section 7.1, we assumed that the discs seen in the BPMG and DEBRIS samples are the same population seen at different ages. While it is possible that the BPMG is representative of the population of stars that become field stars, comparable to the DEBRIS sample, it is also possible that the BPMG and DEBRIS samples do not show the same population of discs.

This could be the case, for example if the discs in the DEBRIS sample are belts of planetesimals like the Edgeworth–Kuiper belt that formed as part of the planet formation process, whereas those in BPMG are remnants of the primordial dust that is swept up into a ring by the depleting gas that forms planetesimals by streaming instability (e.g. Johansen et al. 2007; Johansen, Youdin & Lithwick 2012; Carrera, Johansen & Davies 2015; Carrera et al. 2017; Schaffer, Yang & Johansen 2018). If that is the case, the implication is that BPMG stars would have two belts – the bright primordial dust belt and the DEBRIS-like belt with large planetesimals that may be too faint to detect at this young age. This scenario may be supported by the tentative outer belt found around HD 181327 (e.g. Marino et al. 2017).

However, the planetesimals in the two proposed belts in this scenario would deplete by collisions and thus by  $t^{-1}$  as predicted by collisional models, which is thus incompatible with the rate of  $t^{-2}$  seen in Fig. 10. Nevertheless, a key difference between the two populations might be that the DEBRIS belts would be planetesimals formed in stable regions of the planetary system (like the Edgeworth–Kuiper belt and Asteroid belt), whereas the BPMG belts could be deposited anywhere, since this would depend on how the gas disc depletes, which could be driven by photoevaporation processes. Thus, unstable regions liable to dynamical depletion as discussed in Section 7.1 may be more likely for such BPMG belts.

Another possibility is that the ‘planetesimals’ formed in these unstable regions could be more loosely bound and liable to disruption.

To consider this, we compare the minimum sizes of planetesimals inferred in Section B3 of discs in both the BPMG and DEBRIS samples. Despite the large variation of the sizes, and the small number of discs being compared, we see a similar range between both samples. This does not support the hypothesis of two belts with different planetesimal properties, but it should be noted that if planetesimals form differently, then they may have different  $Q_D^*$  and so different planetesimal sizes would be inferred. Nevertheless, the small planetesimal sizes are in agreement with recent studies suggesting the absence of large planetesimals (Krivov & Wyatt 2021).

Considering the disc radii inferred from spatially resolved images (Section 4), the radii of discs in the BPMG lie between 45 and 94 au. We might expect systematic differences in the disc radius between the BPMG and DEBRIS samples for this scenario. This might be supported by the fact that the spatially resolved discs in DEBRIS tend to be larger than those in the BPMG (see Section 6.6.2). However, while the bright belts seen in the BPMG should be depleted and only the fainter DEBRIS belts remain detectable at DEBRIS ages, both planetesimals rings should be present at BPMG ages.

We investigated the possibility of detecting a DEBRIS-like outer planetesimal belt around a BPMG star with a bright inner belt. We took HD 181327 with its bright ring at 80 au and considered an additional fainter outer belt at 150 au with a width of 46 au similar to that of HD 109085 from the DEBRIS sample. Originally, HD 109085 was observed with ALMA at 880  $\mu$ m and a sensitivity of 30  $\mu$ Jy/beam (Marino et al. 2017) while HD 181327 was observed at a higher spatial resolution and a sensitivity of 27  $\mu$ Jy/beam (see Table 5). The surface brightness of HD 109085 is  $\sim 200$   $\mu$ Jy/beam (fig. 1 in Marino et al. 2017). If the disc was located around HD 181327 and observed with the sensitivity of 27  $\mu$ Jy/beam, we would detect it at a  $0.15\sigma$  level (in each beam). With azimuthal and radial averaging, the detection would reach a  $3.4\sigma$  level with ALMA band 7 for the whole disc. Applying an observational setting like that in Marino et al. (2016) with a lower spatial resolution, we would even reach a level of  $\sim 18\sigma$ .

We do not detect such outer discs in the BPMG (the only exception being HD 181327 for which there is a tentative detection at  $\sim 200$  au). This could either mean those outer belts do not exist or they are too faint to detect at that age (e.g. because the collisional cascade has yet to be fully initiated).

## 7.3 Different star formation environments

The third scenario to explain the higher detection rate supposes that the environment of young moving groups is different to that in which field stars form, such that these regions might be more conducive to the retention of bright discs.

Deacon & Kraus (2020) analysed the binary fraction of open clusters such as the Pleiades and compared it to less dense associations including the BPMG. That study found that the rate of wide multiples (between 300 and 3000 au) is higher in young moving groups (14.6 per cent) than in field stars (7.8 per cent) or open clusters (Hyades, 2.5 per cent), which is in agreement with our results (see Section 2.2). Deacon & Kraus (2020) concluded that the rate of multiple systems might be influenced more strongly by environmental factors than by age, which supports the idea of different formation environments for young moving groups and field stars. It seems that wide separation multiple systems are more effectively formed in less dense regions such as young moving groups. However, as shown by Yelverton et al. (2019), an influence of wide separation binaries on the detection rate of debris discs could not be found so far (Section 2.2).

Of greater importance might be the evolution of multiple stellar systems. Reipurth & Mikkola (2012) and Elliott & Bayo (2016) suggested that the fraction of such systems might decrease over time as the stellar systems become unstable and break up within  $\sim 100$  Myr. It is possible that first, the breakups destroy the debris discs in the system, and secondly, the breakups lead to a higher rate of stellar flybys in the moving group, which truncate and/or deplete the debris discs. As a result, the radii of the discs in the field might be on average smaller and fainter than those in the BPMG.

This idea, however, is not supported by our results on the radial distribution in the BPMG and the DEBRIS where the discs in the DEBRIS tend to be larger than in the BPMG (see Section 6.6.2). Lestrade et al. (2011) investigated the depletion of debris discs due to flybys during the first 100 Myr and found that only high-density regions like Orion with star densities  $> 20\,000\text{ pc}^{-3}$  have a significant impact on the discs. Similarly, Vincke & Pfalzner (2018) analysed the impact of the high-density environment found in open clusters, such as Trumpler 14, on discs and planetary systems. That study found that during the initial phase of evolution, stellar flybys resulted in  $\sim 90$  per cent of discs having a radial extent smaller than 50 au. For  $\sim 47$  per cent of the discs, the radii were even smaller than 10 au. At later evolution stages of the clusters, the discs were barely influenced by stellar interactions. Assuming that field stars formed in dense clusters (Eggen 1958), it is possible that stellar flybys truncated a number of their protoplanetary discs leading to a smaller fraction of debris discs with large radii and/or a lower incidence of debris discs around field stars (Hands et al. 2019). Again, this is not supported by the radii of spatially resolved discs (see Section 6.6.2), but since we analysed only a small number of them around field stars, these might be the ones that were not altered by stellar flybys.

Nevertheless, it might be possible that the detection rate of debris discs around field stars is low from an early phase, since their protoplanetary predecessors were already truncated. In contrast, the discs that formed in less dense regions like the BPMG might retain their high detection rates since stellar flybys are less frequent. This might be observationally testable by comparing disc incidences in Section 6 for different clusters with those of more dense clusters at a comparable age. Recently, Miret-Roig, Huéramo & Bouy (2020) derived a disc detection rate of  $9 \pm 9$  per cent for stars ranging from F5 to K5 in the 30-Myr-old cluster IC 4665 based on Spitzer and WISE data. This is much lower compared to the rates we find for the BPMG and the 45-Myr group (75 per cent and 38 per cent, Table 9). However, we note that the cluster has a distance of 350 pc in contrast to the close-by targets analysed in our study so that many discs might be undetected. A more detailed analysis, for example repeating the analyses of the  $f_d$  versus  $R_{BB}$  parameter space like Section 6.5 for IC 4665, would be needed to draw reliable conclusions on this scenario.

## 8 CONCLUSIONS

In the first part of this study, we analysed a sample of 12 F-type stars in the BPMG and investigated different properties of the systems. In the second part, we compared the results of the BPMG to those of other samples of young moving groups and field stars to analyse possible disc evolution processes.

We found that nine stars in the BPMG possess debris discs leading to a detection rate of 75 per cent. This is significantly higher than found in unbiased samples of field stars where only  $\sim 23$  per cent of the targets show evidence for debris discs (Sibthorpe et al. 2018).

Five out of the nine discs were spatially resolved with either ALMA or VLT/SPHERE allowing us to study their radial and grain-

size distribution in more detail. The disc around HD 164249 was spatially resolved with ALMA for the first time. The disc radii lie between 45 and 94 au and are comparable to the radii found for other debris discs and protoplanetary discs but tend to be slightly smaller compared to spatially resolved discs found in the DEBRIS sample of field stars.

We compared the disc radius to blackbody radius ratio derived from SED modelling to the relation based on *Herschel* data presented in Pawellek & Krivov (2015) and found that the resolved discs in the BPMG possess smaller radii than expected. Since ALMA has a higher spatial resolution than *Herschel*, we inferred the sub-mm disc to blackbody radius ratio – stellar luminosity relation from a sample of ALMA data (Matrà et al. 2018). The resulting relation shows a weaker decrease of the radius ratio with increasing stellar luminosity.

The minimum grain sizes of the SED models are in agreement with the blow-out grain sizes of the discs as we would expect from collisional evolution. The exception is HD 15115 with an  $s_{\min}$  of  $\sim 5\text{ }\mu\text{m}$ , which is also the only disc showing the presence of a warm inner component. This result is somewhat different to earlier studies (Pawellek et al. 2014), which found an average size of  $5\text{ }\mu\text{m}$  for a sample of 34 discs. A reason might be that 66 per cent of those discs were fitted with a warm inner component, but nevertheless, the small  $s_{\min}/s_{\text{blow}}$  ratio indicates that the discs are collisionally very active with high levels of dynamical excitation. However, a more detailed analysis is needed to draw strong conclusions.

We compared the sample of BPMG stars to other young moving groups and old field stars, finding that the detection rate of debris discs is significantly higher in young moving groups than in the field star sample. Furthermore, the discs in the BPMG possess a higher fractional luminosity. From collisional evolution models, we would expect the same discs around older stars to be fainter, which might also cause a lower detection rate. However, applying those models we found that evolving the BPMG sample to DEBRIS ages results in a population with significantly higher detection rate than that observed for the actual DEBRIS sample. We investigated different scenarios explaining this.

In the first scenario, we assumed that the BPMG and the DEBRIS samples show the same disc population at different ages. We found that the observed detection rate could be explained by a delayed ignition of the collisional cascade, but that this option seems unlikely since all discs would need to be delayed by the same  $\sim 20$ -Myr time-scale. A more likely scenario is that additional depleting processes are at work so that the disc evolution cannot be explained by collisional processes alone. Depletion through gravitational interaction with unseen planets is one possibility. We found that Neptune-size planets orbiting within discs can cause depletion on the required  $\sim 100$ -Myr time-scales and are small enough to remain undetected in current observations. For discs close to the star, high-energy stellar flares and other radiation effects (e.g. YORP) are also possible but less likely. Whatever the processes are, they have to work between 10 and 100 Myr since previous studies showed that disc evolution is slower at older ages (e.g. Holland et al. 2017).

The second scenario assumed that the discs in young moving groups and around old field stars are not part of the same population. It is possible that discs in the BPMG possess two belts, one made of large planetesimals formed by planet formation processes comparable to the Edgeworth-Kuiper belt, and another made of remnants of the primordial dust that grow to planetesimal sizes during the disc dispersal process. This might be supported by the different radii found for the BPMG and DEBRIS samples, but since we studied only a small number of discs, the actual radius distribution is not well characterized yet. However, while the two-population scenario



is not impossible, we would still need to invoke a rapid depletion as proposed in the first scenario (Section 7.1).

In the third scenario, we assumed that the birth environment of stars is different for young moving groups and field stars so that their respective discs might be different as well. The influence of stellar flybys in circumstellar discs is significant at early stages of the evolution for dense stellar clusters like Orion (e.g. Lestrade et al. 2011; Vincke & Pfalzner 2018) but barely contributes to the depletion of debris discs found in less dense associations like the BPMG. On the other hand, field stars are supposed to form in regions of higher stellar density so that stellar flybys might truncate the discs at an early evolutionary stage. Therefore, a large fraction of discs around field stars might possess a radius too small to be detected while discs with larger radii in moving groups remain detectable. This is not supported by the radii of spatially resolved discs in the BPMG and the DEBRIS, but it is possible that we see only those discs around field stars that were not truncated. A possibility to test this hypothesis is to analyse the detection rates of debris discs in young dense clusters. Indeed, studies found lower disc detections for the clusters (e.g. IC 4665, Miret-Roig et al. 2020), but this might be biased by the large distance of IC 4665 rather than an actual difference in the fraction of stars with discs.

## ACKNOWLEDGEMENTS

NP thanks Alexander Krivov and Torsten Löhne for fruitful discussions. GMK was supported by the Royal Society as a Royal Society University Research Fellow.

The Combined Atlas of Sources with Spitzer/IRS Spectra (CASIS) is a product of the Infrared Science Center at Cornell University, supported by NASA and JPL.

This paper makes use of the following ALMA data: ADS/JAO.ALMA#2012.1.00437.S, ADS/JAO.ALMA#2013.1.01147.S, ADS/JAO.ALMA#2015.1.00032.S, ADS/JAO.ALMA#2015.1.00633.S, ADS/JAO.ALMA#2016.1.00358.S, ADS/JAO.ALMA#2017.1.00704.S, ADS/JAO.ALMA#2017.1.00200.S. ALMA is a partnership of ESO (representing its member states), NSF (USA), and NINS (Japan), together with NRC (Canada), MOST and ASIAA (Taiwan), and KASI (Republic of Korea), in cooperation with the Republic of Chile. The Joint ALMA Observatory is operated by ESO, AUI/NRAO and NAOJ.

## DATA AVAILABILITY

The data underlying this article will be shared on request to the corresponding author. The ALMA and *Herschel* data are publicly available and can be queried and downloaded directly from the ALMA archive at <https://almascience.nrao.edu/asax/> and from the *Herschel* archive at <http://archives.esac.esa.int/hsa/whsa/>.

## REFERENCES

- Backman D., Paresce F., 1993, in Levy E. H., Lunine J. I., eds, *Protostars and Planets III*. Univ. of Arizona Press, p. 1253
- Bailer-Jones C. A. L., Rybizki J., Fousneau M., Mantelet G., Andrae R., 2018, *AJ*, 156, 58
- Ballering N. P., Rieke G. H., Su K. Y. L., Montiel E., 2013, *ApJ*, 775, 55
- Bell C. P. M., Mamajek E. E., Naylor T., 2015, *MNRAS*, 454, 593
- Benz W., Asphaug E., 1999, *Icarus*, 142, 5
- Beuzit J.-L. et al., 2019, *A&A*, 631, A155
- Bohren C. F., Huffman D. R., 1983, *Absorption and Scattering of Light by Small Particles*. Wiley and Sons, New York, Chichester, Brisbane, Toronto, Singapore
- Booth M. et al., 2013, *MNRAS*, 428, 1263
- Brott I., Hauschildt P. H., 2005, in Turon C., O’Flaherty K. S., Perryman M. A. C., eds, *ESA SP, Vol. 576, The Three-Dimensional Universe with Gaia*. p. 565,
- Burns J. A., Lamy P. L., Soter S., 1979, *Icarus*, 40, 1
- Carpenter J. M. et al., 2008, *ApJS*, 179, 423
- Carrera D., Johansen A., Davies M. B., 2015, *A&A*, 579, A43
- Carrera D., Gorti U., Johansen A., Davies M. B., 2017, *ApJ*, 839, 16
- Chen C. H., Mittal T., Kuchner M., Forrest W. J., Lisse C. M., Manoj P., Sargent B. A., Watson D. M., 2014, *ApJS*, 211, 25
- Choi J., Dotter A., Conroy C., Cantiello M., Paxton B., Johnson B. D., 2016, *ApJ*, 823, 102
- Churcher L., Wyatt M., Smith R., 2011, *MNRAS*, 410, 2
- Cornwell T. J., 2008, *IEEE J. Sel. Top. Signal Process.*, 2, 793
- Cutri R. M. et al., 2003, *2MASS All Sky Catalog of point sources*
- Davenport J. R. A., 2016, *ApJ*, 829, 23
- Deacon N. R., Kraus A. L., 2020, *MNRAS*, 496, 5176
- Dohnanyi J. S., 1969, *J. Geophys. Res.*, 74, 2531
- Draine B. T., 2003, *ARA&A*, 41, 241
- Đurech J. et al., 2018, *A&A*, 609, A86
- Eggen O. J., 1958, *MNRAS*, 118, 65
- Eiroa C. et al., 2013, *A&A*, 555, A11
- Eker Z. et al., 2008, *MNRAS*, 389, 1722
- Elliott P., Bayo A., 2016, *MNRAS*, 459, 4499
- Engler N. et al., 2019, *A&A*, 622, A192
- Faherty J. K., Bochanski J. J., Gagné J., Nelson O., Coker K., Smithka I., Desir D., Vasquez C., 2018, *ApJ*, 863, 91
- Fisher S. R. A., 1956, *The World of Mathematics*, Vol. 3, Simon & Schuster, New York, p. 1514
- Foreman-Mackey D., Hogg D. W., Lang D., Goodman J., 2013, *PASP*, 125, 306
- Foreman-Mackey D. et al., 2019, *J. Open Source Softw.*, 4, 1864
- Fortney J. J., Marley M. S., Saumon D., Lodders K., 2008, *ApJ*, 683, 1104
- Gagné J., Faherty J. K., 2018, *ApJ*, 862, 138
- Gagné J. et al., 2018a, *ApJ*, 856, 23
- Gagné J., Roy-Loubier O., Faherty J. K., Doyon R., Malo L., 2018b, *ApJ*, 860, 43
- Gagné J., Faherty J. K., Mamajek E. E., 2018c, *ApJ*, 865, 136
- Gaia Collaboration, 2018, *A&A*, 616, A1
- Gáspár A., Psaltis D., Rieke G. H., Özel F., 2012, *ApJ*, 754, 74
- Gáspár A., Rieke G. H., Balog Z., 2013, *ApJ*, 768, 25
- Gehrels N., 1986, *ApJ*, 303, 336
- Geiler F., Krivov A. V., Booth M., Löhne T., 2019, *MNRAS*, 483, 332
- Gomes R., Levison H. F., Tsiganis K., Morbidelli A., 2005, *Nature*, 435, 466
- Goodman J., Weare J., 2010, *Commun. Appl. Math. Comput. Sci.*, 5, 65
- Hands T. O., Dehnen W., Gration A., Stadel J., Moore B., 2019, *MNRAS*, 490, 21
- Holland W. S. et al., 2017, *MNRAS*, 470, 3606
- Hughes A. M., Duchêne G., Matthews B. C., 2018, *ARA&A*, 56, 541
- Ishihara D. et al., 2010, *A&A*, 514, A1
- Izidoro A., Morbidelli A., Raymond S. N., 2014, *ApJ*, 794, 11
- Janson M. et al., 2014, *ApJS*, 214, 17
- Johansen A., Oishi J. S., Low M.-M. M., Klahr H., Henning T., Youdin A., 2007, *Nature*, 448, 1022
- Johansen A., Youdin A. N., Lithwick Y., 2012, *A&A*, 537, A125
- Kalas P., Fitzgerald M. P., Graham J. R., 2007, *ApJL*, 661, L85
- Kass R. E., Raftery A. E., 1995, *J. Am. Stat. Assoc.*, 90, 773
- Kenyon S. J., Bromley B. C., 2008, *ApJS*, 179, 451
- Klahr H., Schreiber A., 2020, *ApJ*, 901, 54
- Kovaleva D., Kaygorodov P., Malkov O., Debray B., Oblak E., 2015, *Astron. Comput.*, 11, 119
- Kral Q., Thébaud P., Charnoz S., 2013, *A&A*, 558, A121



- Kral Q., Matra L., Kennedy G., Marino S., Wyatt M., 2020, *MNRAS*, 497, 2811
- Krijt S., Kama M., 2014, *A&A*, 566, L2
- Krivov A. V., 2010, *Res. Astron. Astrophys.*, 10, 383
- Krivov A. V., Wyatt M. C., 2021, *MNRAS*, 500, 718
- Krivov A. V., Löhne T., Sremčević M., 2006, *A&A*, 455, 509
- Krivov A. V., Ide A., Löhne T., Johansen A., Blum J., 2018, *MNRAS*, 474, 2564
- Lebouthier V., Barry D. J., Spoon H. W. W., Bernard-Salas J., Sloan G. C., Houck J. R., Weedman D. W., 2011, *ApJS*, 196, 8
- Lestrade J. F., Morey E., Lassus A., Phou N., 2011, *A&A*, 532, A120
- Levison H. F., Morbidelli A., Vanlaerhoven C., Gomes R., Tsiganis K., 2008, *Icarus*, 196, 258
- Lisse C. M. et al., 2020, *ApJ*, 894, 116
- Löhne T., Krivov A. V., Rodmann J., 2008, *ApJ*, 673, 1123
- Löhne T., Krivov A. V., Kirchschlager F., Sende J. A., Wolf S., 2017, *A&A*, 605, A7
- MacGregor M. A., Wilner D. J., Andrews S. M., Hughes A. M., 2015, *ApJ*, 801, 59
- MacGregor M. A. et al., 2019, *ApJL*, 877, L32
- Macintosh B. et al., 2015, *Science*, 350, 64
- Mamajek E. E., Bell C. P. M., 2014, *MNRAS*, 445, 2169
- Marino S. et al., 2016, *MNRAS*, 460, 2933
- Marino S. et al., 2017, *MNRAS*, 465, 2595
- Marino S. et al., 2018, *MNRAS*, 479, 5423
- Marley M. S., Fortney J. J., Hubickyj O., Bodenheimer P., Lissauer J. J., 2007, *ApJ*, 655, 541
- Marshall J. P., Booth M., Holland W., Matthews B. C., Greaves J. S., Zuckerman B., 2016, *MNRAS*, 459, 2893
- Marton G. et al., 2015, in IAU General Assembly, 29. p. 2253107
- Matrà L., Marino S., Kennedy G. M., Wyatt M. C., Öberg K. I., Wilner D. J., 2018, *ApJ*, 859, 72
- Matrà L., Wyatt M. C., Wilner D. J., Dent W. R. F., Marino S., Kennedy G. M., Milli J., 2019, *AJ*, 157, 135
- Miret-Roig N., Huélamo N., Bouy H., 2020, *A&A*, 641, A156
- Moór A. et al., 2013, *MNRAS*, 435, 1376
- Nesvorný D., 2015, *AJ*, 150, 73
- Nielsen E. et al., 2019, *AJ*, 158, 13
- O'Brien D. P., Greenberg R., 2003, *Icarus*, 164, 334
- Pascucci I. et al., 2006, *ApJ*, 651, 1177
- Patience J. et al., 2015, in AAS/Division for Extreme Solar Systems Abstracts, 47. p. 202.01
- Pawellek N., 2017, PhD thesis, Jena, available at [https://www.db-thueringen.de/receive/dbt\\_mods.00031595](https://www.db-thueringen.de/receive/dbt_mods.00031595)
- Pawellek N., Krivov A. V., 2015, *MNRAS*, 454, 3207
- Pawellek N., Krivov A. V., Marshall J. P., Montesinos B., Ábrahám P., Moór A., Bryden G., Eiroa C., 2014, *ApJ*, 792, 65
- Pawellek N., Moór A., Pascucci I., Krivov A. V., 2019, *MNRAS*, 487, 5874
- Paxton B., Bildsten L., Dotter A., Herwig F., Lesaffre P., Timmes F., 2011, *ApJS*, 192, 3
- Paxton B. et al., 2013, *ApJS*, 208, 4
- Paxton B. et al., 2015, *ApJS*, 220, 15
- Pérez S., Marino S., Casassus S., Baruteau C., Zurlo A., Flores C., Chauvin G., 2019, *MNRAS*, 488, 1005
- Perrot C. et al., 2019, *A&A*, 626, A95
- Phillips N. M., Greaves J. S., Dent W. R. F., Matthews B. C., Holland W. S., Wyatt M. C., Sibthorpe B., 2010, *MNRAS*, 403, 1089
- Rajan A. et al., 2017, *AJ*, 154, 10
- Rebull L. M. et al., 2008, *ApJ*, 681, 1484
- Reipurth B., Mikkola S., 2012, *Nature*, 492, 221
- Ren B. et al., 2019, *ApJ*, 882, 64
- Riviere-Marichalar P. et al., 2014, *A&A*, 565, A68
- Rodriguez D. R., Zuckerman B., 2012, *ApJ*, 745, 147
- Schaffer N., Yang C.-C., Johansen A., 2018, *A&A*, 618, A75
- Schneider J., 2011, in EPSC-DPS Joint Meeting 2011. Nantes, France, p. 3
- Schneider G. et al., 2006, *ApJ*, 650, 414
- Schüppler C., Löhne T., Krivov A. V., Ertel S., Marshall J. P., Eiroa C., 2014, *A&A*, 567, A127
- Sepulveda A. G. et al., 2019, *ApJ*, 881, 84
- Shannon A., Bonsor A., Kral Q., Matthews E., 2016, *MNRAS*, 462, L116
- Shkolnik E. L., Allers K. N., Kraus A. L., Liu M. C., Flagg L., 2017, *AJ*, 154, 69
- Sibthorpe B., Kennedy G. M., Wyatt M. C., Lestrade J. F., Greaves J. S., Matthews B. C., Duchêne G., 2018, *MNRAS*, 475, 3046
- Sierchio J. M., Rieke G. H., Su K. Y. L., Gaspar A., 2014, *ApJ*, 785, 33
- Soumer R. et al., 2014, *ApJL*, 786, L23
- Stark C. C., Schneider G., Weinberger A. J., Debes J. H., Grady C. A., Jang-Condell H., Kuchner M. J., 2014, *ApJ*, 789, 58
- Stern S. A. et al., 2019, in Lunar and Planetary Science Conference. p. 1742
- Stewart S. T., Leinhardt Z. M., 2009, *ApJL*, 691, L133
- Su K. Y. L. et al., 2006, *ApJ*, 653, 675
- Suzuki D. et al., 2016, *ApJ*, 833, 145
- Tazzari M., Beaujean F., Testi L., 2018, *MNRAS*, 476, 4527
- Thebault P., 2016, *A&A*, 587, A88
- Thebault P., Augereau J.-C., 2007, *A&A*, 472, 169
- Tokovinin A. A., 1997, *AApS*, 124, 75
- Torres C. A. O., Quast G. R., Melo C. H. F., Sterzik M. F., 2008, in Reipurth B., ed., *Young Nearby Loose Associations*, 5. p. 757
- Trilling D. E. et al., 2008, *ApJ*, 674, 1086
- Van Doorselaere T., Shariati H., Debusscher J., 2017, *ApJS*, 232, 26
- Vican L., 2012, *AJ*, 143, 135
- Vincke K., Pfalzner S., 2018, *ApJ*, 868, 1
- Wiegert J., Faramaz V., Cruz-Saenz de Miera F., 2016, *MNRAS*, 462, 1735
- Wright E. L. et al., 2010, *AJ*, 140, 1868
- Wyatt M. C., 2008, *ARA&A*, 46, 339
- Wyatt M. C., 2018, *Debris Disks: Probing Planet Formation*. p. 146
- Wyatt M. C., Dent W. R. F., 2002, *MNRAS*, 334, 589
- Wyatt M. C., Smith R., Greaves J. S., Beichman C. A., Bryden G., Lisse C. M., 2007, *ApJ*, 658, 569
- Xuan J. W., Kennedy G. M., Wyatt M. C., Yelverton B., 2020, *MNRAS*, 499, 5059
- Yelverton B., Kennedy G. M., Su K. Y. L., Wyatt M. C., 2019, *MNRAS*, 488, 3588
- Zuckerman B., Rhee J. H., Song I., Bessell M. S., 2011, *ApJ*, 732, 61

## APPENDIX A: SEDS OF DEBRIS DISCS AROUND NEARBY F STARS

### A1 45-Myr group

We analysed the sample of 29 F-type stars found in the 45-Myr group (see Section 6.3) and found that 11 of them exhibit significant mid-infrared excess. We fitted the SEDs of these targets with a modified blackbody model, which is described in detail in Section 3. The results are shown in Fig. A1.

### A2 150-Myr group

We analysed the sample of 13 F-type stars found in the 150-Myr group (see Section 6.3) and found that two of them exhibit significant mid-infrared excess. We fitted the SEDs of these targets with a modified blackbody model, which is described in detail in Section 3. The results are shown in Fig. A2.

### A3 DEBRIS

We analysed the sample of 92 F-type stars in DEBRIS (see Section 6.2) and found that 21 of them exhibit significant mid-infrared excess. We fitted the SEDs of these targets with a modified blackbody model, which is described in detail in Section 3. The results are shown in Figs A3 and A4.

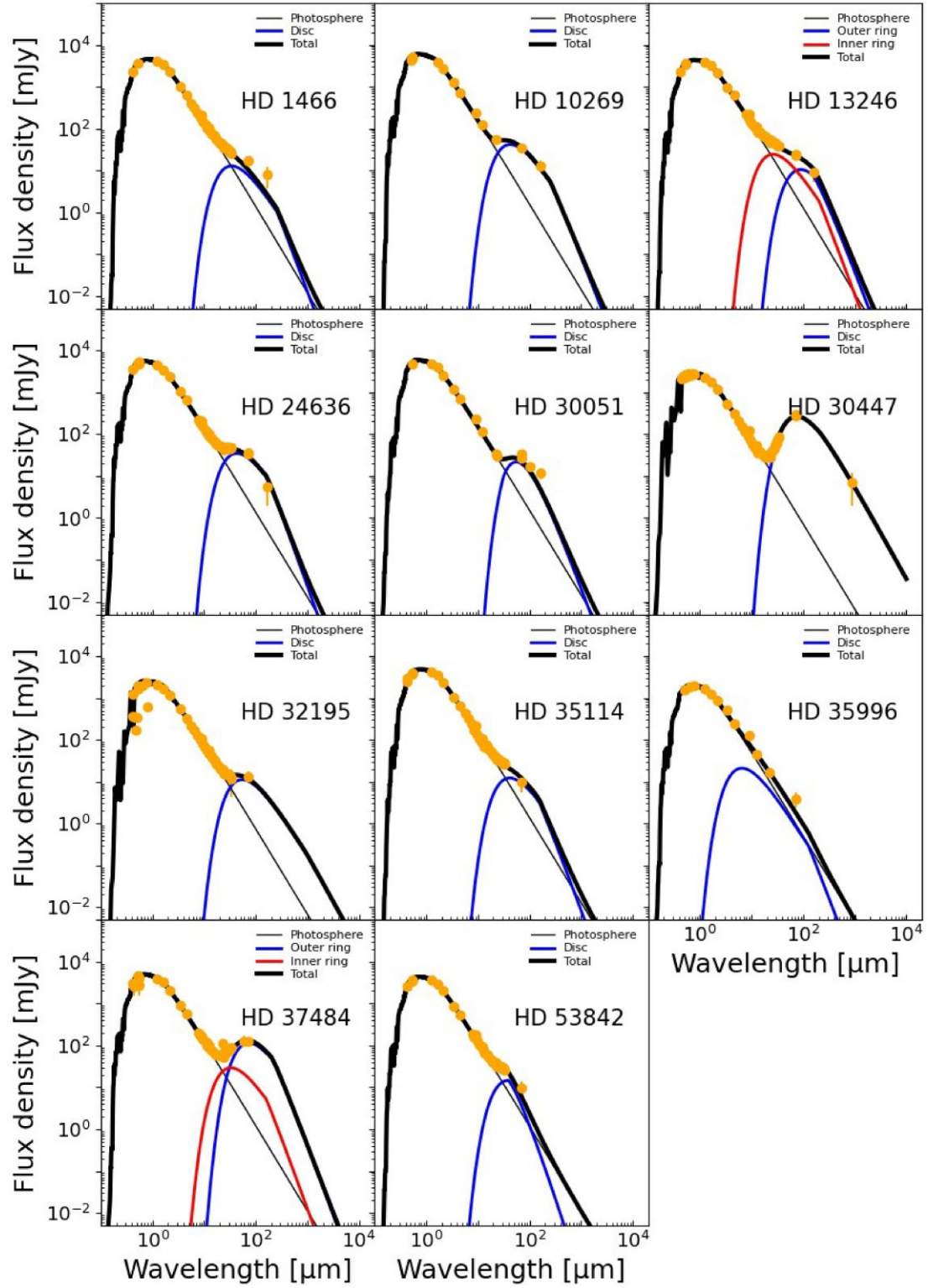


**Figure A1.** SEDs for the debris discs detected around F stars in the 45-Myr group.

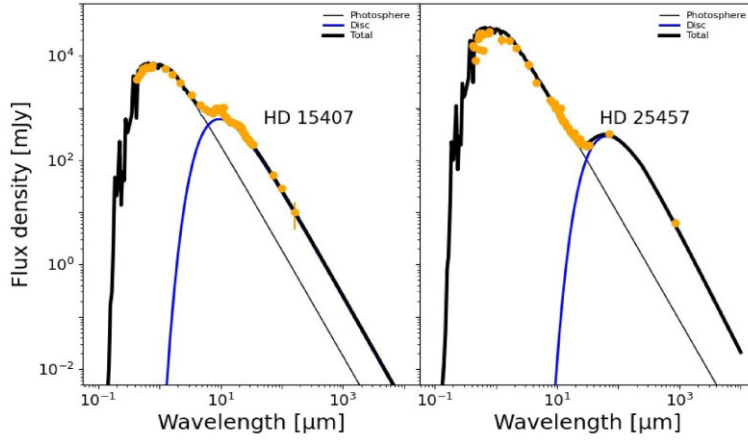


**Figure A2.** SEDs for the debris discs detected around F stars in the 150-Myr group.

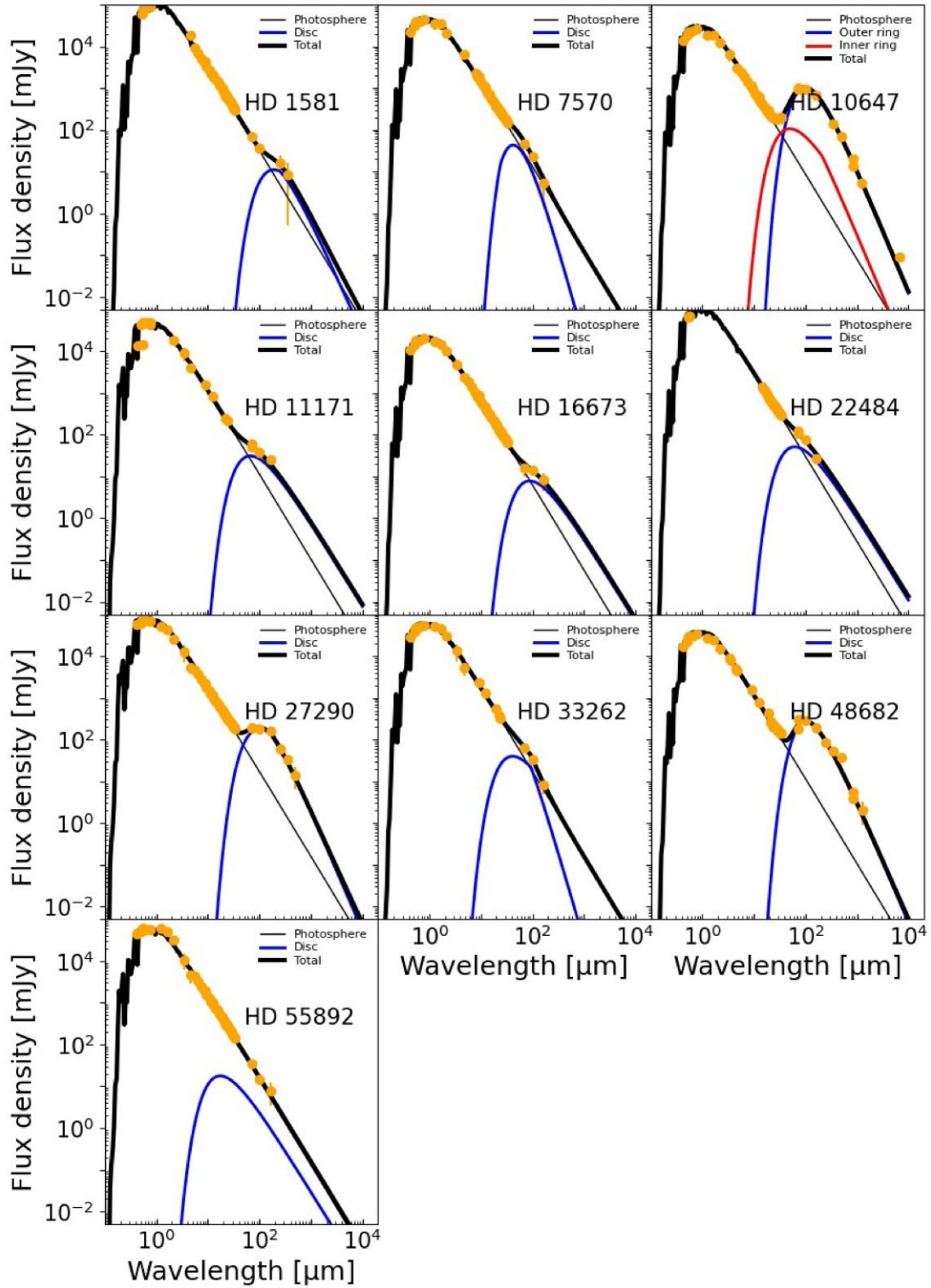


**Figure A3.** SEDs for the debris discs detected around F stars in the DEBRIS sample.



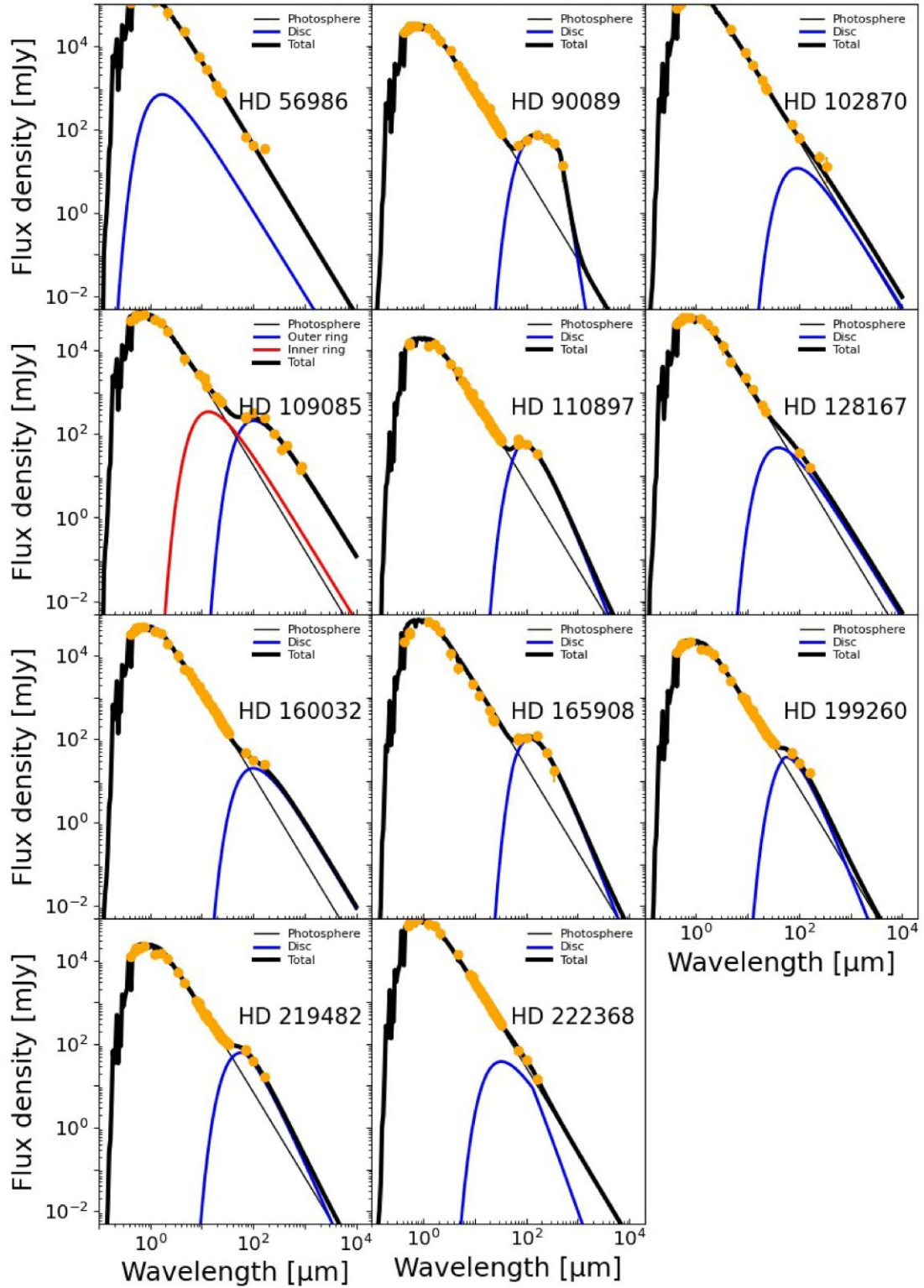


**Figure A4.** SEDs for the debris discs detected around F stars in the DEBRIS sample (continued).

## APPENDIX B: COLLISIONAL DISC EVOLUTION

While we inferred the minimum sizes of dust from SED modelling in Section 5, we can further constrain the size distribution by inferring

the minimum size of the planetesimals that must be feeding the collisional cascade by extrapolating the size distribution of the dust up to the size at which the collisional lifetime is equal to the age of the star, applying the lifetimes calculated using the analytical collision evolution model introduced by Wyatt et al. (2007).

### B1 Collision model

The model uses a similar power-law size distribution as the SED model following

$$N_{\text{coll}}(s) \approx s^{2-3q}, \quad (\text{B1})$$

with  $s$  being the radius of a spherical body and  $N(s)ds$  the number of bodies in the size range  $s$  to  $s + ds$ . We note that the parameter  $q$  is different from the size distribution index inferred by SED modelling (Section 5). They are related by  $q_{\text{SED}} = -(2 - 3q)$  leading to  $q_{\text{SED}} = 3.5$  and  $q = 1.83$  for an ideal collisional cascade (Dohnanyi 1969).

Following equation (12) from Wyatt et al. (2007) and equation (22) from Löhne et al. (2008), we get an equation for the collisional time-scale,  $t_c$ , as a function of minimum size of the planetesimals necessary to feed to collisional cascade,  $s_c$ :

$$t_c = \frac{r^{1/2} dr i}{(\gamma M_{\text{star}})^{1/2} f_d \left(\frac{5}{4}e^2 + i^2\right)^{1/2}} \left(\frac{s_c}{s_{\text{blow}}}\right)^{3q-5} \times \left\{ [X_c^{5-3q} - 1] + 2\frac{q-5/3}{q-4/3} [X_c^{4-3q} - 1] + \frac{q-5/3}{q-1} [X_c^{3-3q} - 1] \right\}^{-1}. \quad (\text{B2})$$

The time-scale depends on the fractional luminosity,  $f_d$ , the blow-out grain size,  $s_{\text{blow}}$ , the stellar mass,  $M_{\text{star}}$ , the disc radius,  $r$ , the disc width,  $dr$ , the eccentricity,  $e$ , the inclination,  $i$ , and the parameter  $X_c$ , which is defined as

$$X_c = \left[ \frac{2Q_D^*}{v_{\text{imp}}^2} \right]^{1/3}. \quad (\text{B3})$$

Here,  $Q_D^*$  is the catastrophic disruption threshold and  $v_{\text{imp}}$  is the impact velocity of the colliding bodies given as  $v_{\text{imp}} = \sqrt{\gamma M_{\text{star}} r^{-1} (5/4e^2 + i^2)}$  with  $\gamma$  as gravitational constant. In the following section, we fix both eccentricity and inclination to a value of 0.1.

### B2 The catastrophic disruption threshold

The collisional time-scale strongly depends on the catastrophic disruption threshold,  $Q_D^*$ , of the planetesimals, which is the specific energy necessary to disperse a target (e.g. Benz & Asphaug 1999). The parameter can be described by a two power-law function taking into account the material strength, the self-gravity of particles, and the impact velocity (Stewart & Leinhardt 2009):

$$Q_D^* = \left[ A \left( \frac{s}{1\text{cm}} \right)^a + B \left( \frac{s}{1\text{cm}} \right)^b \right] (v_{\text{imp}})^k. \quad (\text{B4})$$

The parameters  $A$ ,  $B$ ,  $a$ ,  $b$ , and  $k$  are material constants. We found that  $v_{\text{imp}}$  is on average  $\sim 0.4 \text{ km s}^{-1}$  for the discs in our samples assuming that  $e = i = 0.1$ . Following O'Brien & Greenberg (2003), we can infer the size distribution index,  $q_{\text{SED}}$ , from  $Q_D^*$  using the parameter  $a$  from equation (B4):

$$q_{\text{SED}} = \frac{7 + a/3}{2 + a/3}. \quad (\text{B5})$$

Hence, not only the collisional time-scale but also the size distribution of planetesimals depends on  $Q_D^*$ .

Studies of the collisional evolution of debris discs (e.g. Wyatt & Dent 2002; Schüppler et al. 2014; Löhne et al. 2017; Krivov et al. 2018; Geiler et al. 2019) often assume the materials 'sand' (Stewart &

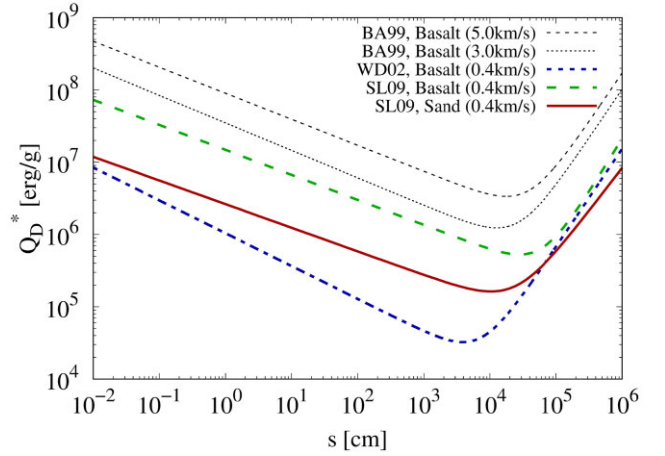


**Figure B1.**  $Q_D^*$  as function of size. The thin black dashed and dotted lines show values for basalt at 3 and 5  $\text{km s}^{-1}$  taken from Benz & Asphaug (1999). The parameters of the HD 109085 system are assumed. The thick blue dash-dotted line shows the scaling result taken for Wyatt & Dent (2002) and the thick green dashed line shows the lab results taken from Stewart & Leinhardt (2009) for basalt at 0.4  $\text{km s}^{-1}$ . The thick solid red line shows the result for 'sand' at 0.4  $\text{km s}^{-1}$  taken from Stewart & Leinhardt (2009).

Leinhardt 2009) and basalt (Benz & Asphaug 1999). In Fig. B1,  $Q_D^*$  is depicted as a function of size for both materials. Using equation (B4), we find that the values for basalt colliding at 0.4  $\text{km s}^{-1}$  lie one order of magnitude below those of Benz & Asphaug (1999) colliding at 5  $\text{km s}^{-1}$ .

Another approach to infer values of  $Q_D^*$  at the appropriate impact velocity is given by Wyatt & Dent (2002), which introduced a scaling method where  $Q_D^* \propto v_{\text{imp}}^\delta$ . Here,  $\delta$  is found by comparing the two impact velocity curves given in Benz & Asphaug (1999). The method gives values one order of magnitude below those from Stewart & Leinhardt (2009) for sizes smaller than  $\sim 100 \text{ m}$  (strength regime). For larger sizes ( $\sim 1 \text{ km}$ , gravity regime), the values are comparable to each other. The results using sand as material at 0.4  $\text{km s}^{-1}$  lie between those of basalt from Wyatt & Dent (2002) and Stewart & Leinhardt (2009) and show a flatter decrease than basalt in the strength regime. The values in the gravity regime are close to those of basalt, but the increase is flatter.

The approaches of Wyatt & Dent (2002) and Stewart & Leinhardt (2009) to scale  $Q_D^*$  to the impact velocity are both used in the literature. Therefore, we emphasize that  $Q_D^*$  strongly depends on the method applied and shows variations of one order of magnitude even for the same material. Furthermore,  $Q_D^*$  varies for the material chosen.

### B3 Minimum sizes of planetesimals feeding the cascade

We calculate the minimum sizes of the planetesimals feeding the collisional cascade using equation (B2) assuming that the collisional time-scale,  $t_c$ , is similar to the age of the system.

Table B1 lists the planetesimal sizes and the corresponding minimum disc masses (since the size distribution must extend up to these sizes and could extend further) assuming the two different approaches to scale  $Q_D^*$  to the impact velocity of the colliding bodies as well as the two materials basalt and sand. We added the discs HD 10647 and HD 109085 from the DEBRIS sample to compare the planetesimal sizes in systems of different age. Both discs were spatially resolved with ALMA.

**Table B1.** Sizes of planetesimals.

HD	System parameters						Basalt (WD02)		Basalt (SL09)		Sand (SL09)	
	$r$ (au)	$dr$ (au)	$M_{\text{star}}$ ( $M_{\odot}$ )	$s_{\text{blow}}$ ( $\mu\text{m}$ )	$f_d$	$t_c$ (Myr)	$s_c$ (m)	$M_{\text{disc}}$ ( $M_{\text{earth}}$ )	$s_c$ (m)	$M_{\text{disc}}$ ( $M_{\text{earth}}$ )	$s_c$ (m)	$M_{\text{disc}}$ ( $M_{\text{earth}}$ )
15115	93	21	1.37	0.91	$5.3 \times 10^{-4}$	23	338	23	104	7.0	381	26
160305	88	4	1.13	0.67	$1.5 \times 10^{-4}$	23	351	6.0	115	2.0	401	6.9
164249	63	24	1.30	0.89	$9.4 \times 10^{-4}$	23	514	28	413	23	678	37
181327	81	16	1.36	1.02	$4.1 \times 10^{-3}$	23	1417	562	1601	634	2188	867
191089	45	16	1.36	0.98	$1.6 \times 10^{-3}$	23	1105	53	1310	63	1703	81
10647	82	49	1.12	0.48	$2.9 \times 10^{-4}$	1000	960	28	1006	29	1405	40
109085	152	46	1.53	1.24	$1.7 \times 10^{-5}$	1000	239	1.4	19	0.11	213	1.2

*Note.* The system data for HD 10647 were taken from Lovell et al. (in preparation), the data for HD 109085 from Matrà et al. (2018). The age estimates for both stars show large uncertainties so that we fix the age to 1000 Myr for simplicity reasons. ‘Basalt (WD02)’ refers to the scaling method of  $Q_D^*$  used in Wyatt & Dent (2002) while ‘Basalt (SL09)’ assumes the velocity dependence found in Stewart & Leinhardt (2009). ‘Sand (SL09)’ refers to the weak rock material introduced in Stewart & Leinhardt (2009).

We find that the smallest planetesimals feeding the collisional cascade show sizes from several metres up to  $\sim 2$  kilometres independently of the age of the system. For some discs, this is somewhat smaller than assumed by former studies, which found sizes around kilometres (e.g. Wyatt & Dent 2002; Marino et al. 2017; Krivov et al. 2018). This is also smaller than the predicted sizes of hundreds of kilometres from planetesimal formation scenarios (e.g. Klahr & Schreiber 2020) and might indicate a lack of those large planetesimals as was proposed by Krivov & Wyatt (2021).

However, we find that the discs analysed show variations of sizes of one order of magnitude for all materials. Applying equation (B4), the maximum sizes using basalt are smaller than those using sand. While for large planetesimals in the gravity regime the differences between the materials are small, they become more pronounced for metre-size planetesimals close to the strength regime similar to the trend of  $Q_D^*$  shown in Fig. B1. Considering the two scaling methods, we find a comparable trend – the method chosen to infer  $Q_D^*$  becomes more important for smaller sizes.

The large variation in sizes leads to different disc masses depending on the material applied. Again, discs for which the planetesimals feeding the dust belt are only required to be metre in size are more sensitive to the material and method used. The masses vary between  $2M_{\oplus}$  (HD 160305) and  $900M_{\oplus}$  (HD 181327).

Studies of planetesimal formation (e.g. Klahr & Schreiber 2020) found that typical planetesimal sizes tend to decrease with increasing distance to the star and with the time of the formation of planetesimals. While an early formation might lead to sizes of  $\sim 100$  km, planetesimals formed at a later stage tend to be as small as  $\sim 10$  km (e.g. Stern et al. 2019). This is still somewhat larger than the sizes of  $\sim 1$  km we infer for our discs, but we note that our estimated sizes are minimum sizes necessary to feed the collisional cascade.

This paper has been typeset from a  $\text{\LaTeX}$  file prepared by the author.